

Electronic supplementary information (ESI)

Work function and *d*-band center dual-modulation in hollow Ru-ZIF-8-derived Ru⁰-RuO₂-ZnO heterointerfaces for boosted electrochemical hydrogen evolution

Xiaoxin Xu, Ruidong Shi, Yuanting Li, Xue Wang, Gongbing Zhou*

Chongqing Key Laboratory of Inorganic Functional Materials, College of Chemistry,
Chongqing Normal University, Chongqing 401331, P. R. China.

* Corresponding author. *E-mail*: gbzhou@cqnu.edu.cn

1. Materials

Zinc acetate dihydrate ($\text{Zn}(\text{CH}_3\text{COO})_2 \cdot 2\text{H}_2\text{O}$) was obtained from Aladdin Reagent Co. Ltd., China. 2-Methylimidazole (98%), cetyltrimethylammonium bromide (CTAB, 99%), ruthenium(III) chloride trihydrate (98%), and Nafion solution (5 wt%) were provided by Adamas-Beta. Methanol (99.5%, AR) and ethanol (99.7%, AR) were sourced from Chengdu Kelong Chemical Reagent. Nickel foam (NF) with a thickness of 1 mm was supplied by Kunshan Guangjiayuan New Material Co. Ltd., China. Glassy carbon electrode with a diameter of 3 mm was supplied by Gooss Union. Hydrochloric acid (35 wt%, AR) was purchased from Chongqing Chuandong Chemical Co. Ltd., China. Potassium hydroxide (KOH, 90%, AR) was acquired from General Reagent. The 20 wt% Pt/C catalyst was supplied by Shanghai Hesun Electric Co. Ltd., China. Argon (Ar, 99.999%) and hydrogen (H_2 , 99.999%) were provided by Chongqing Ruike Gas Co., China. The Graphite rod (99.995% purity, 5 mm in diameter, with an ash content of 50 ppm), Ag/AgCl (3.5 mol L^{-1} KCl), Hg/HgO (1 mol L^{-1} KOH), and Pt plate electrodes (99.99% purity) were obtained from Tianjin AIDA Science-Technology Development Co. Ltd., China.

2. Characterizations

Scanning electron microscopy (SEM) images were acquired using a field-emission scanning electron microscope (Hitachi SU8010). Powder X-ray diffraction (XRD) was performed on a Bruker AXS D8 Advance X-ray diffractometer, utilizing Ni-filtered Cu $K\alpha$ radiation ($\lambda = 0.15418 \text{ nm}$). The operating conditions were set to 40 kV for the tube voltage and 30 mA for the current, with a scanning rate of 2° min^{-1} . Inductively coupled plasma–atomic emission spectroscopy (ICP–AES) was carried out using a Thermo Elemental IRIS Intrepid system. Raman spectra were recorded on a HORIBA JY LabRAM HR Evolution Raman spectrometer with 532 nm laser excitation. Electron paramagnetic resonance (EPR) spectra were collected at room temperature using a Bruker E500 spectrometer. Fourier transform infrared (FTIR) spectra were conducted with a SHIMADZU FTIR-8400s spectrometer over the range of $4000\text{--}400 \text{ cm}^{-1}$ at a resolution of 4 cm^{-1} , averaging 32 scans per measurement. N_2 physisorption analysis was

performed using an Autosorb-IQ physisorption analyzer (Anton Paar), with sample pretreatment at 150 °C for 6 h under flowing N₂ (99.999%).

Transmission electron microscopy (TEM) images, high-resolution TEM (HRTEM) images, and high-angle annular dark-field scanning transmission electron microscopy (HAADF-STEM) images were obtained using a field-emission transmission electron microscope (FEI Tecnai G2 S-Twin F20) equipped with an energy-dispersive X-ray analyzer (EDX; Oxford INCA) for elemental mapping.

X-ray photoelectron spectra (XPS) and Auger electron spectra (AES) were collected using a Thermo Escalab 250Xi spectrometer with Al K α radiation ($h\nu = 1486.6$ eV) as the excitation source. The as-synthesized material was mounted on the sample stage, degassed overnight at room temperature in the pretreatment chamber under vacuum, and subsequently transferred to the analyzing chamber, where the background pressure was maintained below 1×10^{-8} mbar. The pass energy and step size were set to 100 eV and 1 eV, respectively, for the survey spectra, and to 30 eV and 0.1 eV, respectively, for the core-level spectra. All spectra were calibrated against the graphite carbon 1s peak at a binding energy (BE) of 284.5 eV.

3. Electrochemical measurements

The electrocatalytic hydrogen evolution reaction (HER) performances of the as-synthesized nanocrystals were evaluated using a CHI760E electrochemical workstation (CH Instrument Inc.) with a three-electrode cell. The Hg/HgO (1 mol L⁻¹ KOH) electrode and a graphite rod were used as the reference and counter electrodes, respectively, while the synthesized nanocrystals, cut to a size of 1 cm \times 1 cm, served as the working electrodes. Prior to electrochemical testing, the electrolyte (1 mol L⁻¹ KOH) was saturated by N₂, followed by cyclic voltammetry (CV) scanning for 30 cycles over a potential window of -0.8 to -1.5 V versus Hg/HgO (1 mol L⁻¹ KOH) at a scanning rate of 100 mV s⁻¹ to activate the electrode and achieve a steady state. Linear sweep voltammetry (LSV) scanning was then conducted under the same potential window and N₂ atmosphere at room temperature, with a scanning rate of 5 mV s⁻¹,

to determine the overpotentials (η) at different current densities (j). The Tafel constant (a) and the Tafel slope (b) were obtained by fitting the equation $\eta = a + blgj$.

Potential calibrations: To measure the potential difference between the Hg/HgO (1 mol L⁻¹ KOH) reference electrode and the reversible hydrogen electrode (RHE), CV scans were conducted in 1 mol L⁻¹ KOH at a scan rate of 1 mV s⁻¹. A Pt plate (1 cm² immersed in the solution) was used as both the working and counter electrodes. The electrolyte was purged with H₂ (99.999%) before and during the CV scan process. For the obtained CV curve (Fig. S7), the potential at which the current crossed zero was regarded as the thermodynamic potential for the hydrogen electrode reactions.¹ The average value of these two potentials (-0.9295 V) was adopted to calibrate the potential. The compensated potential was determined using iR_s -correction (90%),^{2,3} based on the solution resistance (R_s) derived from electrochemical impedance spectroscopy tests. As a result, all measured electrode potentials relative to the Hg/HgO reference electrode ($E_{vs. Hg/HgO}$) were calibrated to RHE using the equation $E_{RHE-corrected} = E_{vs. Hg/HgO} + 0.9295 - 0.9iR_s$.

Electrochemical impedance spectroscopy (EIS) measurements: The R_s and charge transfer resistance (R_{ct}) of the synthesized materials were obtained from EIS measurements conducted at an operation potential of -0.1 V versus RHE, across a frequency range of 10 kHz to 0.01 Hz.

Electrochemical active surface area (ECSA) measurements: The ECSAs of the synthesized nanocrystals were estimated based on the double-layer capacitance (C_{dl}) using the equation:⁴

$$ECSA = \frac{C_{dl}}{C_s} \times s = \frac{\Delta j}{2\nu C_s} \times s$$

where C_{dl} was measured by CV tests at different scanning rates (ν , 20 to 100 mV s⁻¹) over a potential window from 0.10 to 0.20 V relative to RHE. C_s is the average general-specific capacitance (0.04 mF cm⁻² in 1.0 mol L⁻¹ KOH).⁴ s represents the geometric area of the working electrode (1 cm²). Δj is the difference between anodic and cathodic current densities.

Turnover frequency (TOF) calculations: The intrinsic HER activities of the synthesized nanocrystals were expressed by the TOF of H₂ generation, calculated based on the assumption that all Ru atoms are active sites and accessible to the electrolyte:⁵⁻⁷

$$TOF = \frac{\text{Total hydrogen turnovers per geometric area}}{\text{Active sites per geometric area}}$$

The total hydrogen turnovers were calculated from the current density using the following equation:⁵

$$\begin{aligned} & \text{Total hydrogen turnovers per geometric area} \\ &= \left(|j| \frac{\text{mA}}{\text{cm}^2} \right) \left(\frac{1 \text{ C s}^{-1}}{1000 \text{ mA}} \right) \left(\frac{1 \text{ mol e}^-}{96485.3 \text{ C}} \right) \left(\frac{1 \text{ mol H}_2}{2 \text{ mol e}^-} \right) \left(\frac{6.022 \times 10^{23} \text{ H}_2 \text{ molecules}}{1 \text{ mol H}_2} \right) \\ &= |j| \times 3.12 \times 10^{15} \left(\frac{\text{H}_2 / \text{s}}{\text{cm}^2} \right) \end{aligned}$$

where j is the current density (mA cm^{-2}).

The total active sites per geometric area were calculated according to the following equation:

$$\text{Active sites per geometric area} = \frac{m_{\text{Ru}} (\text{g cm}^{-2})}{M_{\text{Ru}} (\text{g mol}^{-1})} \times N_A (\text{mol}^{-1})$$

where m_{Ru} is the Ru mass obtained by ICP–AES, M_{Ru} is the molar mass of Ru, and N_A is Avogadro constant ($6.022 \times 10^{23} \text{ mol}^{-1}$).

For d-Ru-ZnO-880:

$$\begin{aligned} & \text{Active sites per geometric area} \\ &= \left(\frac{m_{\text{d-Ru-ZnO-880}} (\text{mg cm}^{-2}) \times \text{Ru (wt\%)} }{M_{\text{Ru}} (\text{g mol}^{-1})} \right) / 1000 (\text{mg g}^{-1}) \times N_A (\text{mol}^{-1}) \\ &= \left(\frac{1 \times 8.8\%}{101.07} \right) / 1000 \times 6.022 \times 10^{23} \frac{\text{active sites}}{\text{cm}^2} \\ &= 5.24 \times 10^{17} \frac{\text{active sites}}{\text{cm}^2} \end{aligned}$$

For d-Ru-ZnO-900:

$$\begin{aligned} & \text{Active sites per geometric area} \\ &= \left(\frac{m_{\text{d-Ru-ZnO-900}} (\text{mg cm}^{-2}) \times \text{Ru (wt\%)} }{M_{\text{Ru}} (\text{g mol}^{-1})} \right) / 1000 (\text{mg g}^{-1}) \times N_A (\text{mol}^{-1}) \\ &= \left(\frac{1 \times 11.5\%}{101.07} \right) / 1000 \times 6.022 \times 10^{23} \frac{\text{active sites}}{\text{cm}^2} \\ &= 6.85 \times 10^{17} \frac{\text{active sites}}{\text{cm}^2} \end{aligned}$$

For d-Ru-ZnO-920:

Active sites per geometric area

$$\begin{aligned}
 &= \left(\frac{m_{d-Ru-ZnO-920} \text{ (mg cm}^{-2}\text{)} \times Ru \text{ (wt\%)} \right) / 1000 \text{ (mg g}^{-1}\text{)} \times N_A \text{ (mol}^{-1}\text{)} \\
 &= \left(\frac{1 \times 8.2\%}{101.07} \right) / 1000 \times 6.022 \times 10^{23} \frac{\text{active sites}}{\text{cm}^2} \\
 &= 4.89 \times 10^{17} \frac{\text{active sites}}{\text{cm}^2}
 \end{aligned}$$

Therefore, the TOFs of H₂ generation over the electrocatalysts in HER were acquired by the following formulas:

For d-Ru-ZnO-880:

$$\begin{aligned}
 TOF &= \left(|j| \times 3.12 \times 10^{15} \right) / \left(5.24 \times 10^{17} \right) \frac{H_2 / s}{\text{active sites}} \\
 &= 5.95 \times 10^{-3} \times |j| \frac{H_2 / s}{\text{active sites}}
 \end{aligned}$$

For d-Ru-ZnO-900:

$$\begin{aligned}
 TOF &= \left(|j| \times 3.12 \times 10^{15} \right) / \left(6.85 \times 10^{17} \right) \frac{H_2 / s}{\text{active sites}} \\
 &= 4.55 \times 10^{-3} \times |j| \frac{H_2 / s}{\text{active sites}}
 \end{aligned}$$

For d-Ru-ZnO-920:

$$\begin{aligned}
 TOF &= \left(|j| \times 3.12 \times 10^{15} \right) / \left(4.89 \times 10^{17} \right) \frac{H_2 / s}{\text{active sites}} \\
 &= 6.38 \times 10^{-3} \times |j| \frac{H_2 / s}{\text{active sites}}
 \end{aligned}$$

Apparent activation energy (E_a) calculations. The E_a values of the synthesized nanocrystals in HER were determined by fitting the slope of the Arrhenius plot ($\lg|j_0| - 1/T$) based on the Arrhenius relationship:⁷

$$\frac{\partial \lg|j_0|}{\partial(1/T)} = - \frac{E_a}{2.303R}$$

where j_0 is the exchange current density obtained by extrapolating the abscissa of the $E_{RHE\text{-corrected}} - \lg|j|$ curve to zero $E_{RHE\text{-corrected}}$. R is the ideal gas constant (8.314 J mol⁻¹ K⁻¹), and T is the testing temperature (303, 313, 323, and 333 K). Due to the instability of the Hg/HgO (1 mol L⁻¹ KOH) and graphite rod electrodes at elevated temperature, Ag/AgCl (3.5 mol L⁻¹ KCl)

and a Pt plate were used as the reference and counter electrodes, respectively, in the E_a testing experiments. Similar to the $E_{vs. Hg/HgO}$ potential calibration, the measured $E_{vs. Ag/AgCl}$ potentials using the Ag/AgCl (3.5 mol L⁻¹ KCl) reference electrode were calibrated to RHE with a $0.9iR_s$ -correction using the following equations (Fig. S14):

$$303 \text{ K: } E_{\text{RHE-corrected}} = E_{\text{vs. Ag/AgCl}} + 1.0090 - 0.9iR_s$$

$$313 \text{ K: } E_{\text{RHE-corrected}} = E_{\text{vs. Ag/AgCl}} + 1.0110 - 0.9iR_s$$

$$323 \text{ K: } E_{\text{RHE-corrected}} = E_{\text{vs. Ag/AgCl}} + 1.0120 - 0.9iR_s$$

$$333 \text{ K: } E_{\text{RHE-corrected}} = E_{\text{vs. Ag/AgCl}} + 1.0100 - 0.9iR_s$$

Stability testing: The durability of the synthesized nanocrystals in HER was evaluated by recording current–time (i – t) curves at potentials corresponding to current densities of 10 and 100 mA cm⁻² using a single-port electrolytic cell.

Faraday efficiency (FE) calculation: The FE was calculated using the equation:¹

$$FE = \frac{n_{\text{ex}}}{n_{\text{th}}} \times 100\%$$

where n_{ex} is the experimentally produced moles of H₂, and n_{th} is the theoretically produced moles of H₂. n_{ex} is obtained by dividing the measured volume of H₂ using a water drainage method by 22.4 L mol⁻¹. n_{th} is calculated by $n_{\text{th}} = Q/2F$, with Q being calculated by integrating the corresponding i - t curve and F being the Faraday constant (96485.3 C mol⁻¹).

4. Determination of exposed facets on ZnO, RuO, and RuO₂

(1) Hexagonal RuO and ZnO

For hexagonal crystals, the crystal plane angle (ϕ) can be calculated using the following equation:

$$\cos \phi = \frac{h_1 h_2 + k_1 k_2 + 0.5(h_1 k_2 + h_2 k_1) + \frac{3a^2}{4c^2} l_1 l_2}{\sqrt{\left(h_1^2 + k_1^2 + h_1 k_1 + \frac{3a^2}{4c^2} l_1^2\right) \left(h_2^2 + k_2^2 + h_2 k_2 + \frac{3a^2}{4c^2} l_2^2\right)}}$$

Ru⁰ in *d*-Ru-ZnO-880 and *d*-Ru-ZnO-920: For hexagonal Ru⁰, the lattice constants (JCPDS 06-0663) are $a = 2.706 \text{ \AA}$, $b = 2.706 \text{ \AA}$, $c = 4.282 \text{ \AA}$, $a/c = 0.632$, $\alpha = 90^\circ$, $\beta = 90^\circ$, $\gamma = 120^\circ$. According

to HRTEM, Ru⁰ in *d*-Ru-ZnO-880 and *d*-Ru-ZnO-920 was enclosed by the (101), ($\bar{1}0\bar{1}$), ($\bar{1}01$), ($10\bar{1}$), (002), and (00 $\bar{2}$) planes, with the zone axis along the [010] direction. Assuming the exposed crystal plane is (*h k l*) and is perpendicular to the zone axis, the angles formed by the (*h k l*) plane and the (101), ($\bar{1}01$), and (002) planes are all 90°, i.e., $\phi = 90^\circ$. Thus, we have:

$$\begin{cases} h + 0.5k + 0.30l = 0 \\ -h - 0.5k + 0.30l = 0 \\ 0.60l = 0 \end{cases}$$

The equation set solution reveals the relationship $2h = -k$ and $l = 0$, indicating that the exposed facets of Ru⁰ are $\{1\bar{2}0\}$.

Ru⁰ in *d*-Ru-ZnO-900: According to HRTEM, Ru⁰ in *d*-Ru-ZnO-900 was enclosed by the (101), ($\bar{1}0\bar{1}$), ($\bar{1}02$), ($10\bar{2}$), (003), and (00 $\bar{3}$) planes, with the zone axis along the [010] direction. Assuming the exposed crystal plane is (*h k l*) and is perpendicular to the zone axis, the angles formed by the (*h k l*) plane and the (101), ($\bar{1}02$), and (003) planes are all 90°, i.e., $\phi = 90^\circ$. Thus, we have:

$$\begin{cases} h + 0.5k + 0.30l = 0 \\ -h - 0.5k + 0.60l = 0 \\ 0.90l = 0 \end{cases}$$

The equation set solution reveals the relationship $2h = -k$ and $l = 0$, indicating that the exposed facets of Ru⁰ are $\{1\bar{2}0\}$.

ZnO in *d*-Ru-ZnO-880: The lattice constants of hexagonal ZnO (JCPDS 36-1451) are $a = 3.250$ Å, $b = 3.250$ Å, $c = 5.207$ Å, $a/c = 0.624$, $\alpha = 90^\circ$, $\beta = 90^\circ$, $\gamma = 120^\circ$. According to HRTEM, ZnO in *d*-Ru-ZnO-880 was enclosed by the (101), ($\bar{1}0\bar{1}$), ($\bar{1}03$), ($10\bar{3}$), (004), and (00 $\bar{4}$) planes, with the zone axis along the [010] direction. Assuming the exposed crystal plane is (*h k l*) and is perpendicular to the zone axis, the angles formed by the (*h k l*) plane and the (101), ($\bar{1}03$), and (004) planes are all 90°, i.e., $\phi = 90^\circ$. Thus, we have:

$$\begin{cases} h + 0.5k + 0.29l = 0 \\ -h - 0.5k + 0.87l = 0 \\ 1.16l = 0 \end{cases}$$

The equation set solution reveals the relationship $2h = -k$ and $l = 0$, indicating that the exposed facets of ZnO are $\{1\bar{2}0\}$.

ZnO in *d*-Ru-ZnO-900 and *d*-Ru-ZnO-920: Similarly, according to HRTEM, ZnO in *d*-Ru-ZnO-900 and *d*-Ru-ZnO-920 was enclosed by the (010), ($0\bar{1}0$), (100), ($\bar{1}00$), (110), and ($\bar{1}10$) planes, with the zone axis along the [001] direction. Assuming the exposed crystal plane is ($h k l$) and is perpendicular to the zone axis, the angles formed by the ($h k l$) plane and the (010), (100), and (110) planes are all 90° , i.e., $\phi = 90^\circ$. Thus, we have:

$$\begin{cases} k + 0.5h = 0 \\ h + 0.5k = 0 \\ 1.5h + 1.5k = 0 \end{cases}$$

The equation set solution reveals the relationship $h = k = 0$, indicating that the exposed facets of ZnO are {001}.

(2) Tetragonal RuO₂

For tetragonal crystals, ϕ can be calculated using the following equation:

$$\cos \phi = \frac{\frac{h_1 h_2 + k_1 k_2}{a^2} + \frac{l_1 l_2}{c^2}}{\sqrt{\left(\frac{h_1^2 + k_1^2}{a^2} + \frac{l_1^2}{c^2}\right) \left(\frac{h_2^2 + k_2^2}{a^2} + \frac{l_2^2}{c^2}\right)}}$$

The lattice constants of tetragonal RuO₂ (JCPDS 40-1290) are $a = 4.499 \text{ \AA}$, $b = 4.499 \text{ \AA}$, $c = 3.107 \text{ \AA}$, $a/c = 1.448$, $\alpha = 90^\circ$, $\beta = 90^\circ$, $\gamma = 90^\circ$. According to HRTEM, RuO₂ in *d*-Ru-ZnO-880, *d*-Ru-ZnO-900, and *d*-Ru-ZnO-920 was enclosed by the (110), ($\bar{1}10$), (101), ($\bar{1}0\bar{1}$), (211), and ($\bar{2}\bar{1}\bar{1}$) planes, with the zone axis along the $[\bar{1}11]$ direction. Assuming the exposed crystal plane is ($h k l$) and is perpendicular to the zone axis, the angles formed by the ($h k l$) plane and the (110), (101), and (211) planes are all 90° , i.e., $\phi = 90^\circ$. Thus, we have:

$$\begin{cases} \frac{h+k}{20.24} = 0 \\ \frac{h}{20.24} + \frac{l}{9.65} = 0 \\ \frac{2h+k}{20.24} + \frac{l}{9.65} = 0 \end{cases}$$

The equation set solution reveals the relationship $h = -k \approx -2l$, indicating that the exposed facets of RuO₂ are $\{\bar{2}21\}$.

5. Density functional theory (DFT) calculations

All DFT calculation were performed using the Vienna Ab initio Simulation Package (VASP).^{8,9} The electron exchange and correlation were described using the generalized gradient approximation (GGA) with the Perdew-Burke-Ernzerhof (PBE) functional.¹⁰ To account for strongly correlated effect, the Hubbard U ($U_{\text{Ru}} = 3$ eV) was applied to the d -orbital.¹¹ Van der Waals interactions were incorporated using the DFT-D3 method developed by Grimme et al. for dispersion correction.¹²

For the bulk optimization of Ru and ZnO, the cutoff energies for the plane wave basis sets were set to 500 eV and 600 eV, respectively.^{13,14} Brillouin zone integration was conducted using a $12 \times 12 \times 6$ Monkhorst-Pack grid k -points for bulk Ru and a $12 \times 12 \times 5$ grid for ZnO. Convergence in electronic self-consistent field cycles was considered achieved when the energy change was less than 1×10^{-6} eV. During the geometry optimization of bulk Ru and ZnO, the maximum force was limited to 0.01 eV \AA^{-1} . Fig. S4 and Table S4 detail the structural changes of bulk Ru and ZnO before and after the geometry optimization, which served as the basis for constructing all slab models.

For all slab surface models (parameters detailed in Table S5), a cutoff energy of 450 eV was used for the plane wave basis set. A $2 \times 2 \times 1$ Monkhorst-Pack grid k -points was employed for Brillouin zone integration. Electronic self-consistent field cycles were considered convergent when the energy change was less than 1×10^{-5} eV. A vacuum region of 15 \AA separated the repeating slabs, with all atomic layers fully relaxed during geometry optimizations. To obtain accurate band structures, convergence criteria were tightened, with electronic self-consistent field cycles considered convergent when the energy change was less than 1×10^{-6} eV. The detailed band gap scanning path in the Brillouin zone is shown in Table S6.

Charge density redistribution between Ru and ZnO layers ($\Delta\rho(Ru-ZnO)$), adsorbed H₂O and slab ($\Delta\rho(H_2O)$), and adsorbed H* and slab ($\Delta\rho(H^*)$) were analyzed using electronic charge density difference (CDD), given by:

$$\begin{aligned}\Delta\rho(Ru-ZnO) &= \rho_{slab} - \rho_{Ru} - \rho_{ZnO} \\ \Delta\rho(H_2O) &= \rho_{slab+H_2O} - \rho_{slab} - \rho_{H_2O} \\ \Delta\rho(H^*) &= \rho_{slab+H^*} - \rho_{slab} - \rho_{H^*}\end{aligned}$$

where ρ_{slab} , ρ_{Ru} , ρ_{ZnO} , ρ_{slab+H_2O} , ρ_{H_2O} , ρ_{slab+H^*} , and ρ_{H^*} are the charge densities of the isolated slab, the Ru layer in the slab, the ZnO layer in the slab, the slab after adsorbing H₂O, the isolated H₂O fragment, the slab after adsorbing H*, and the isolated H* fragment, respectively. The transferred charges of Ru layer and H* were calculated by comparing the corresponding Bader charges.

The work function, defined as the energy required to remove an electron from the surface of a condensed solid into the external vacuum, was calculated using the following equation:¹⁵

$$Work\ Function = E_{vacuum} - E_{Fermi}$$

where E_{vacuum} is the energy level in the vacuum obtained from the electrostatic potential, and E_{Fermi} is the Fermi energy obtained from the density of states (DOS).

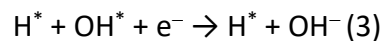
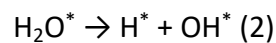
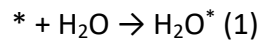
The *d*-band center (ϵ_d) is defined as:¹⁶

$$\epsilon_d = \frac{\int_{-\infty}^{\infty} n_d(\epsilon)\epsilon d\epsilon}{\int_{-\infty}^{\infty} n_d(\epsilon)d\epsilon}$$

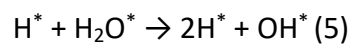
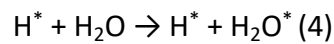
where $n_d(\epsilon)$ and ϵ represent the electronic density and energy of the *d* orbital, respectively.

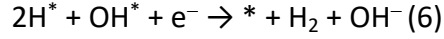
HER that follows the Volmer-Heyrovsky mechanism involves the following processes:¹⁷

Volmer process:



Heyrovsky process:





where the symbol “*” represents an adsorption site, H_2O^* , H^* , and OH^* represent adsorbed intermediates.

The Gibbs free energy change in each HER step (ΔG) was calculated using the equation:

$$\Delta G = \Delta E + \Delta ZPE - T\Delta S$$

where ΔE is the energy change obtained from geometry optimization, and ΔZPE and ΔS are the zero-point energy change and entropy change determined from the computed vibrational frequencies at $T = 298.15$ K.¹⁸ As a result, ΔG for the above steps can be calculated by:

$$\Delta G_1 = E(\text{H}_2\text{O}^*) - E(*) - E(\text{H}_2\text{O}) + (\Delta ZPE - T\Delta S)_1$$

$$\Delta G_2 = E(\text{H}^* + \text{OH}^*) - E(\text{H}_2\text{O}^*) + (\Delta ZPE - T\Delta S)_2$$

$$\Delta G_3 = E(\text{H}^*) + E(\text{OH}^-) - E(\text{H}^* + \text{OH}^*) + (\Delta ZPE - T\Delta S)_3$$

$$\Delta G_4 = E(\text{H}^* + \text{H}_2\text{O}^*) - E(\text{H}^*) - E(\text{H}_2\text{O}) + (\Delta ZPE - T\Delta S)_4$$

$$\Delta G_5 = E(2\text{H}^* + \text{OH}^*) - E(\text{H}^* + \text{H}_2\text{O}^*) + (\Delta ZPE - T\Delta S)_5$$

$$\Delta G_6 = E(*) + E(\text{H}_2) + E(\text{OH}^-) - E(2\text{H}^* + \text{OH}^*) + (\Delta ZPE - T\Delta S)_6$$

where $E(*)$, $E(\text{H}_2\text{O}^*)$, $E(\text{H}^* + \text{OH}^*)$, $E(\text{H}^* + \text{H}_2\text{O}^*)$, $E(2\text{H}^* + \text{OH}^*)$ and $E(\text{H}^*)$ are the computed energies of pure surface and the surface after adsorbing H_2O^* , $\text{H}^* + \text{OH}^*$, $\text{H}^* + \text{H}_2\text{O}^*$, $2\text{H}^* + \text{OH}^*$, and H^* , respectively. $E(\text{H}_2\text{O})$ and $E(\text{H}_2)$ are the computed energies of H_2O and H_2 molecules, respectively. $E(\text{OH}^-)$ is the energy of OH^- obtained from the thermodynamic relation of $\text{H}_2\text{O} = 2\text{H}^+ + \text{OH}^-$.

The adsorption behaviors of H on different computational models were studied by comparing the Gibbs free energy change of H^* adsorption (ΔG_{H^*}), calculated using the following equation:¹⁹

$$\Delta G_{\text{H}^*} = E_{\text{slab} + \text{H}} - E_{\text{slab}} - 1/2E_{\text{H}_2} + \Delta ZPE - T\Delta S$$

where $E_{\text{slab} + \text{H}}$, E_{slab} , and E_{H_2} are the slab energy after adsorbing H, the slab energy, and the energy of a free hydrogen molecule, respectively. The zero-point energy change (ΔZPE) and entropy change (ΔS) were determined from the computed vibrational frequencies at $T = 298.15$ K.¹⁸

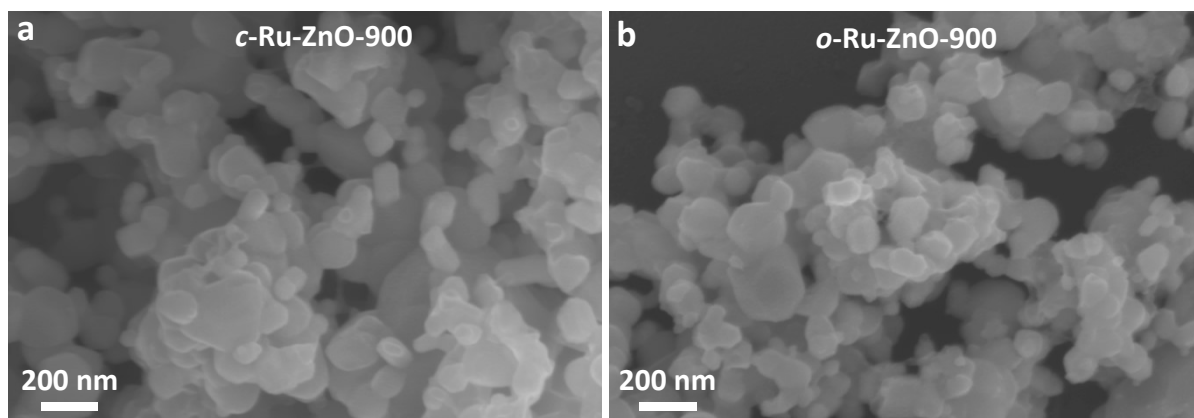


Fig. S1 SEM images of (a) *c*-Ru-ZnO-900 and (b) *o*-Ru-ZnO-900.

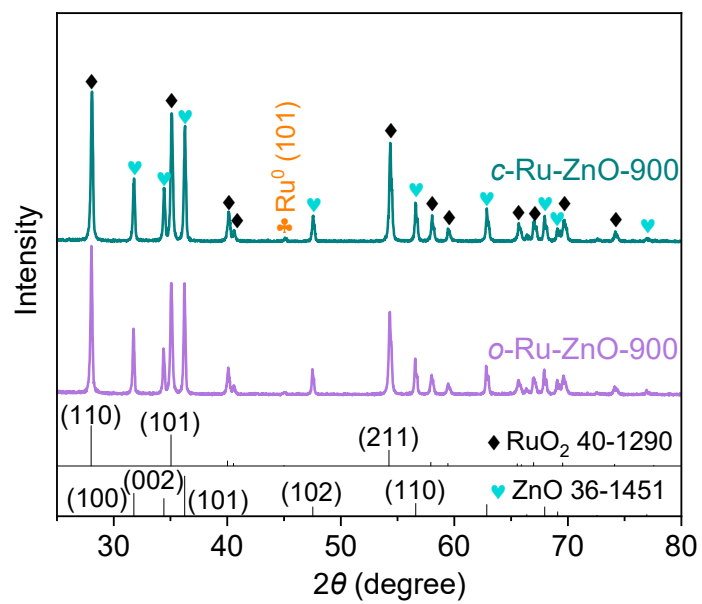


Fig. S2 Powder XRD patterns of c-Ru-ZnO-900 and o-Ru-ZnO-900.

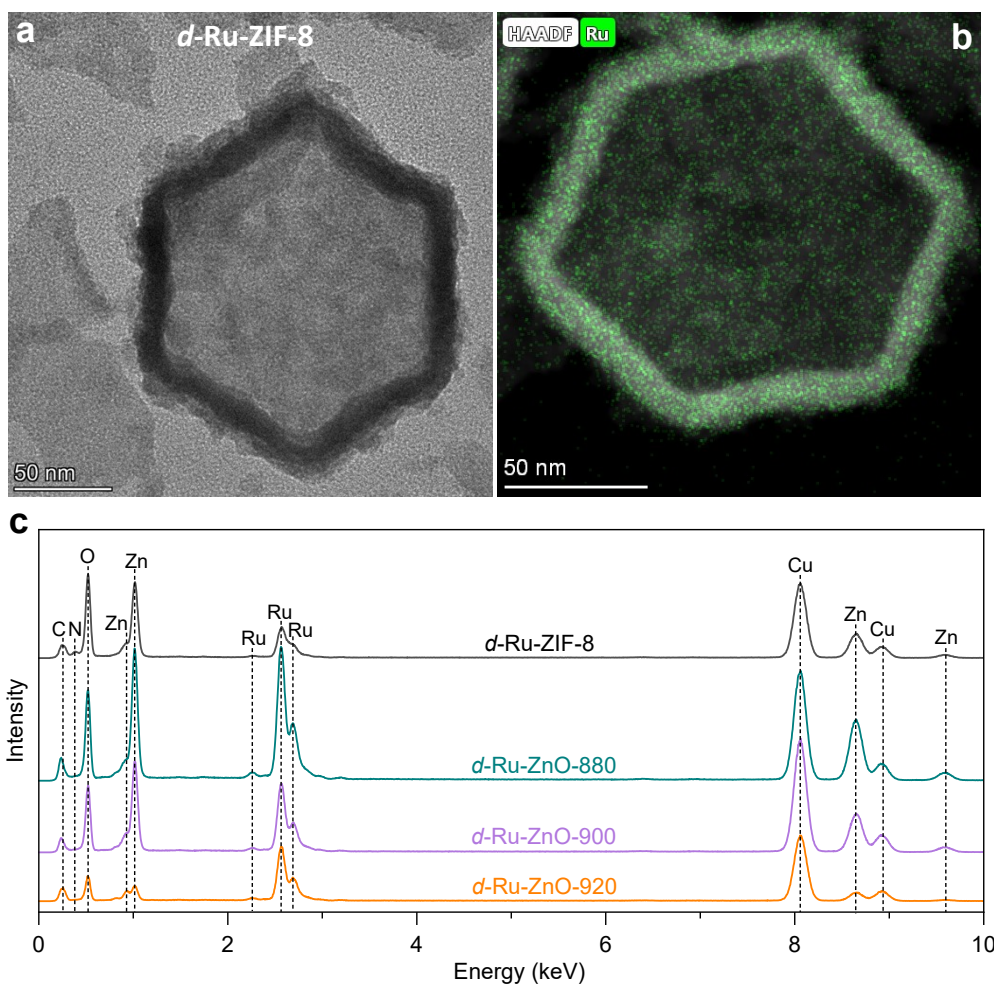


Fig. S3 (a) TEM image of *d*-Ru-ZIF-8; (b) Ru HAADF-STEM image of *d*-Ru-ZIF-8; (c) EDX spectra of *d*-Ru-ZIF-8, *d*-Ru-ZnO-880, *d*-Ru-ZnO-900, and *d*-Ru-ZnO-920.

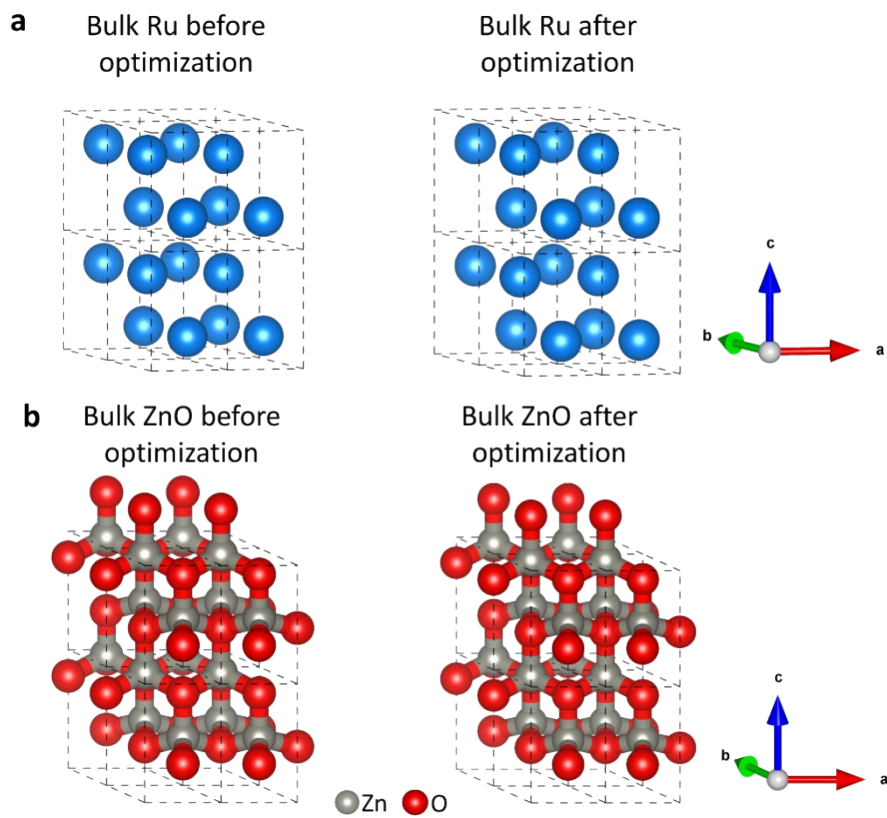


Fig. S4 Crystal structure of bulk (a) Ru and (b) ZnO before and after geometric optimization.

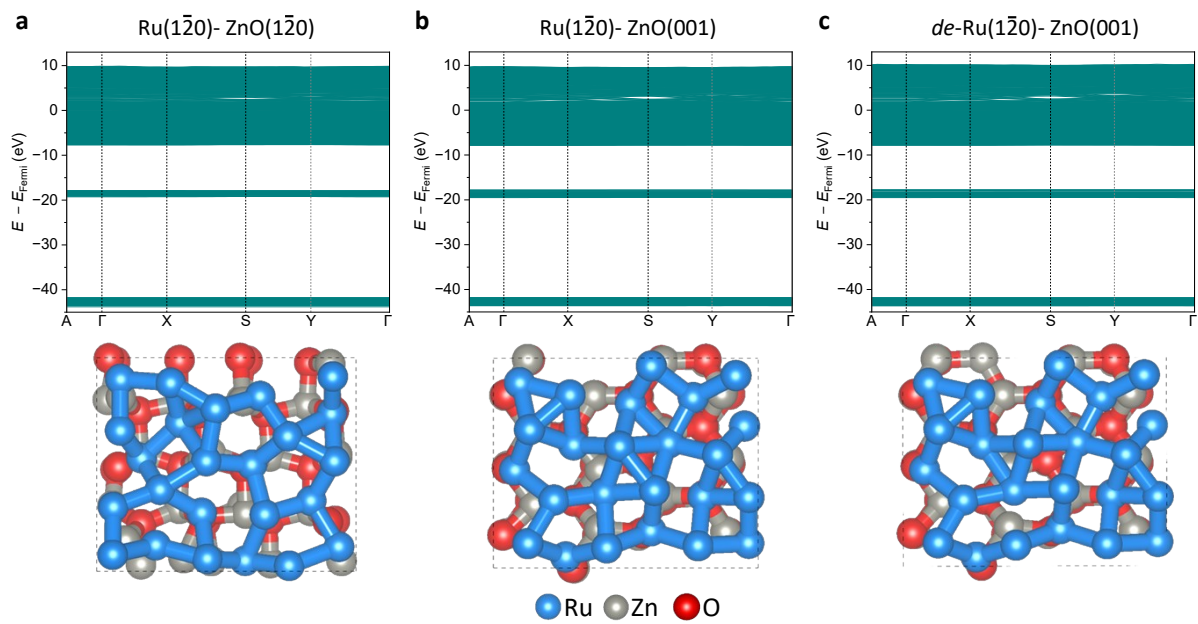


Fig. S5 Band gaps and corresponding top view of optimized configurations of (a) $\text{Ru}(1\bar{2}0)\text{-ZnO}(1\bar{2}0)$, (b) $\text{Ru}(1\bar{2}0)\text{-ZnO}(001)$, and (c) $de\text{-Ru}(1\bar{2}0)\text{-ZnO}(001)$ models.

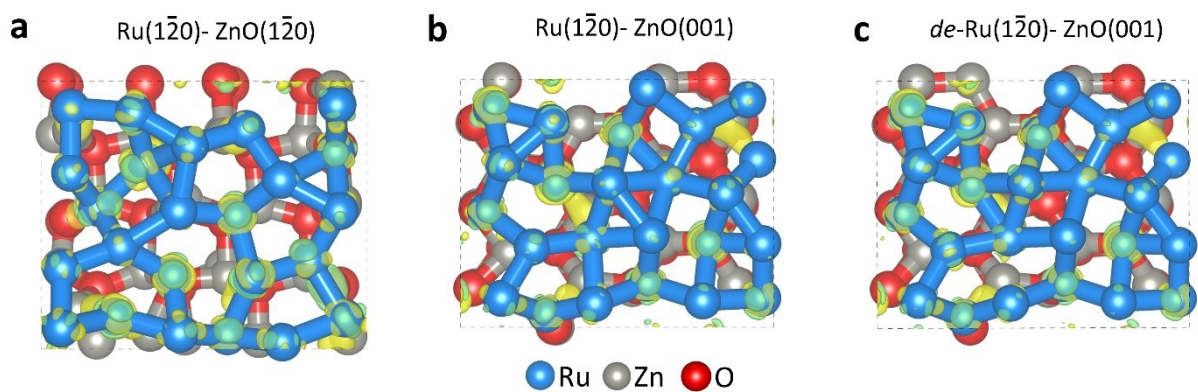


Fig. S6 Top view of differential charge densities of (a) Ru($1\bar{2}0$)-ZnO($1\bar{2}0$), (b) Ru($1\bar{2}0$)-ZnO(001), and (c) *de*-Ru($1\bar{2}0$)-ZnO(001) models after geometric optimization. Isosurface = $\pm 0.008 e \text{ \AA}^{-3}$. Yellow and green regions represent electron accumulation and depletion, respectively.

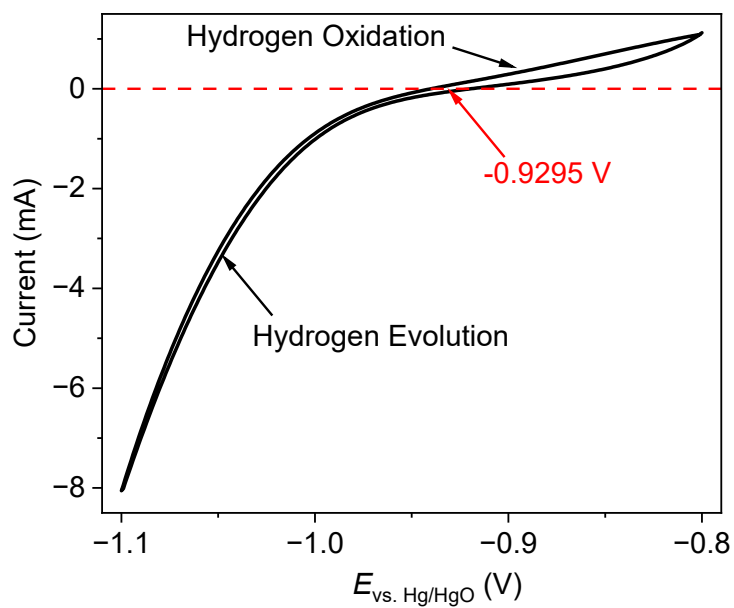


Fig. S7 RHE calibration result of Hg/HgO (1 mol L^{-1} KOH) reference electrode in 1 mol L^{-1} KOH at a scan rate of 1 mV s^{-1} using a Pt plate (1 cm^2 dipped into the solution) as working and counter electrodes.

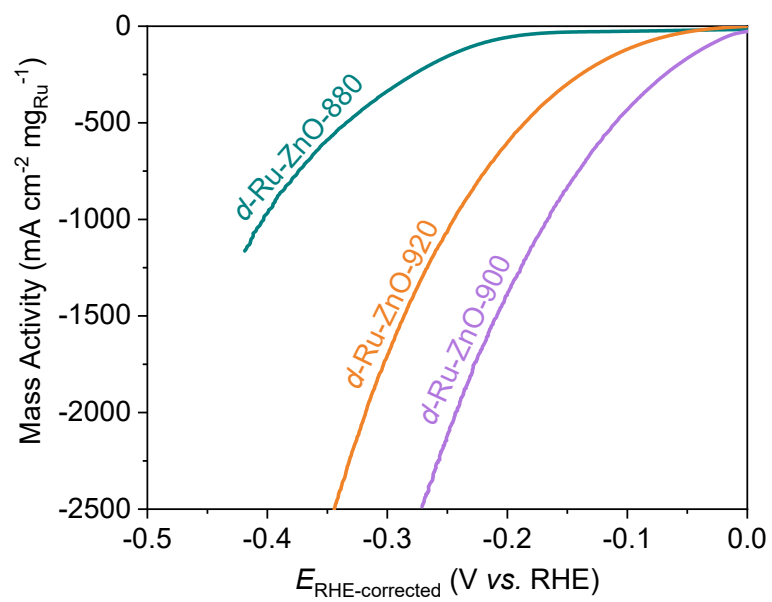


Fig. S8 Mass activity of *d*-Ru-ZnO-880, *d*-Ru-ZnO-900, and *d*-Ru-ZnO-920 in HER.

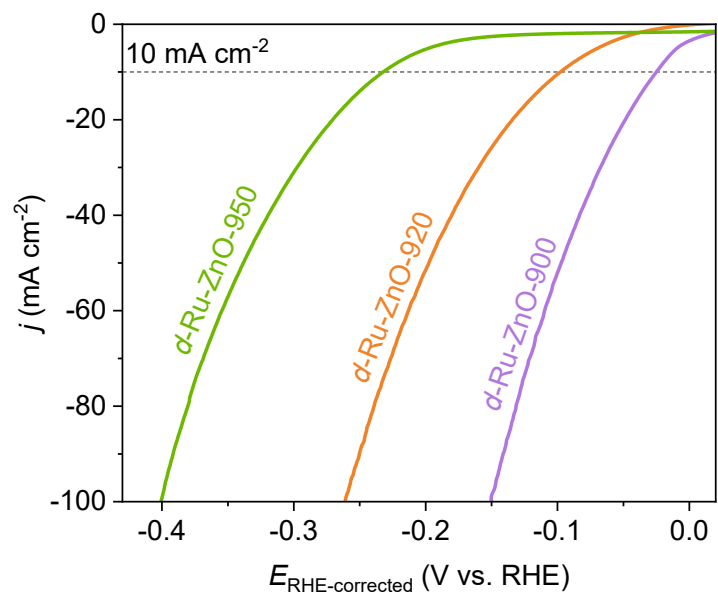


Fig. S9 LSV curves of $d\text{-Ru-ZnO-900}$, $d\text{-Ru-ZnO-920}$, and $d\text{-Ru-ZnO-950}$ towards HER in 1 mol L^{-1} KOH at a scan rate of 5 mV s^{-1} .

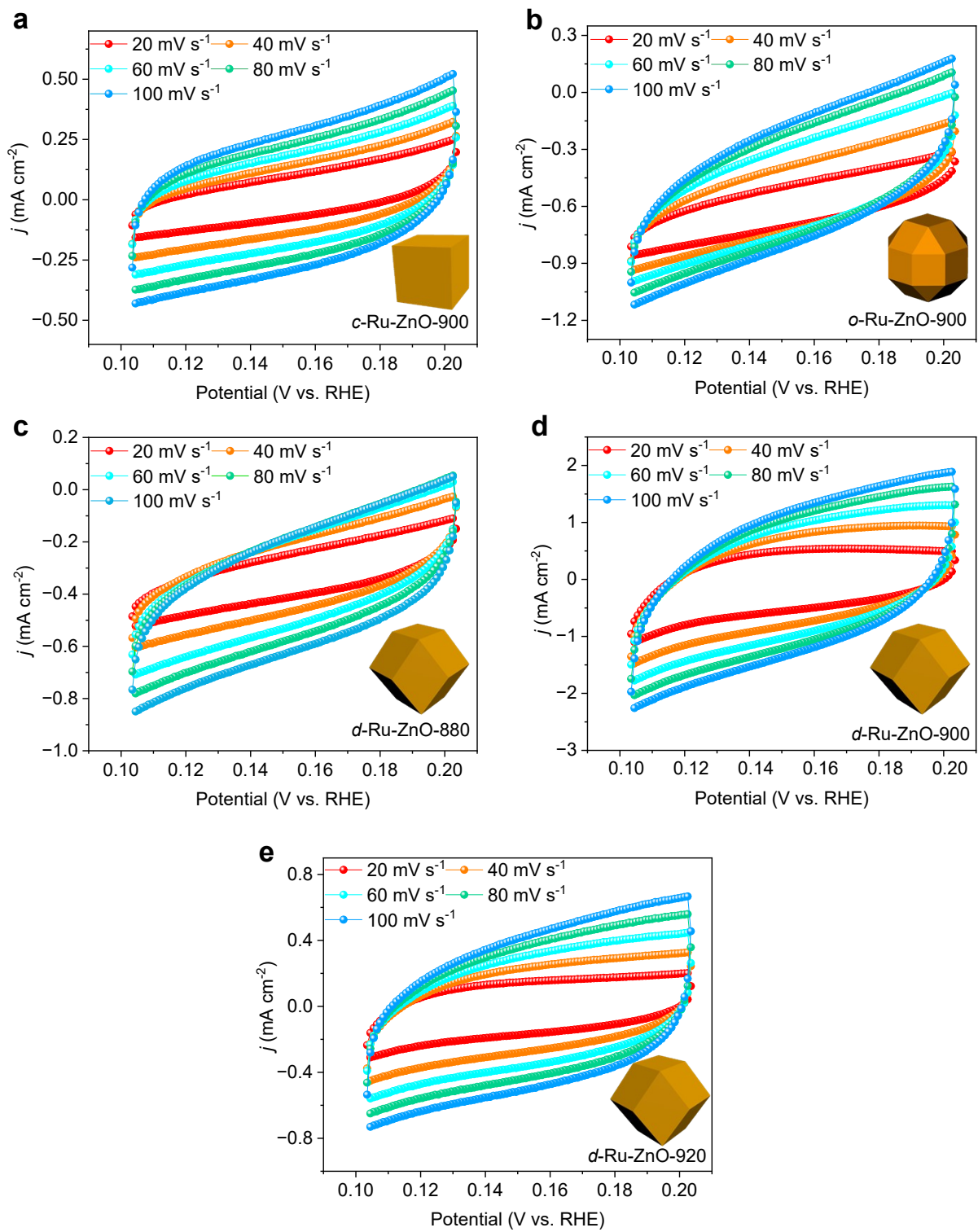


Fig. S10 Cyclic voltammograms at a scan rate of 20, 40, 60, 80, and 100 mV s^{-1} on (a) $c\text{-Ru-ZnO-900}$, (b) $o\text{-Ru-ZnO-900}$, (c) $d\text{-Ru-ZnO-880}$, (d) $d\text{-Ru-ZnO-900}$, and (e) $d\text{-Ru-ZnO-920}$.

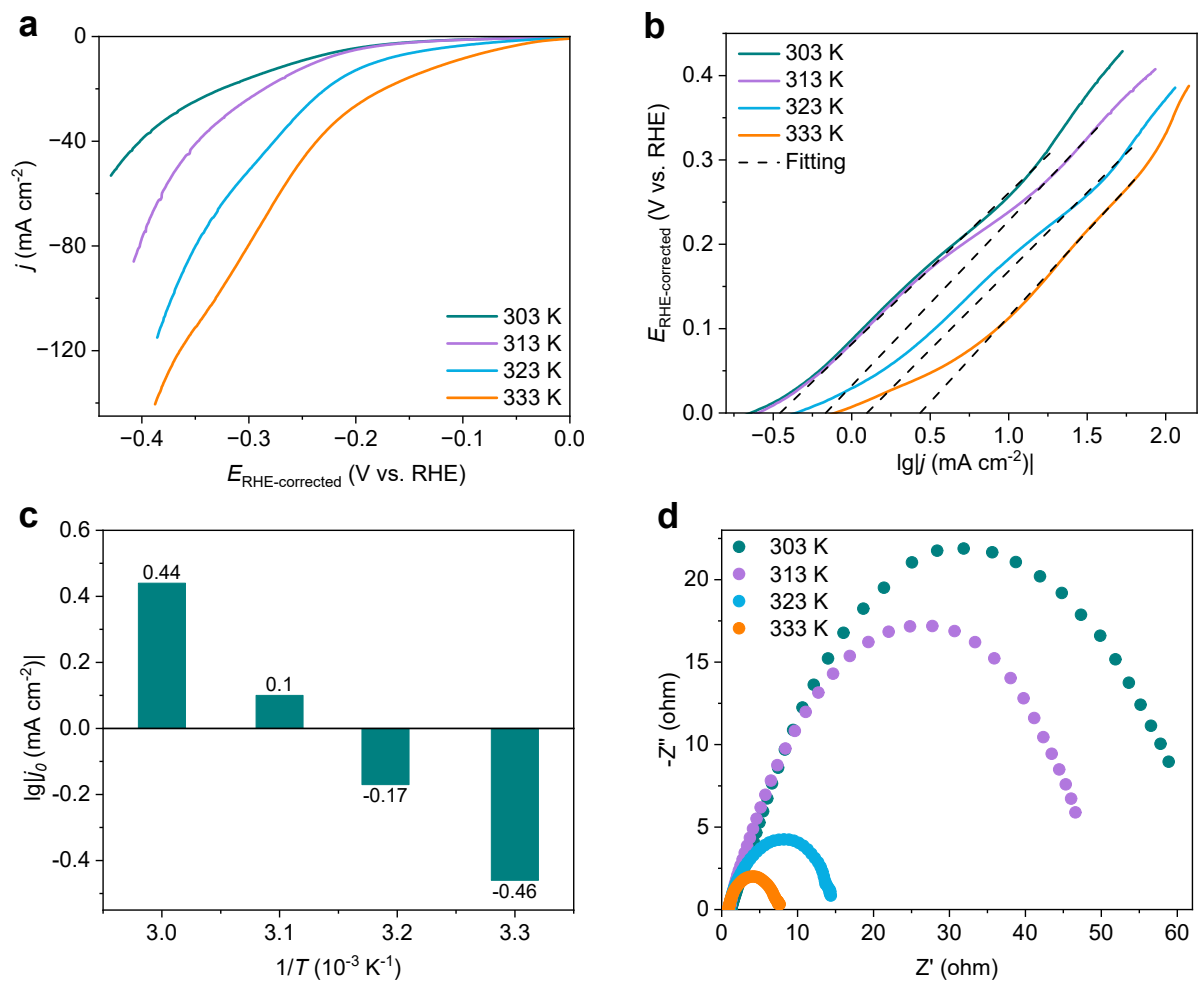


Fig. S11 (a) LSV curves, (b) Tafel plots, (c) exchange current densities, and (d) Nyquist plots of *d*-Ru-ZnO-880 in HER at 303, 313, 323, and 333 K.

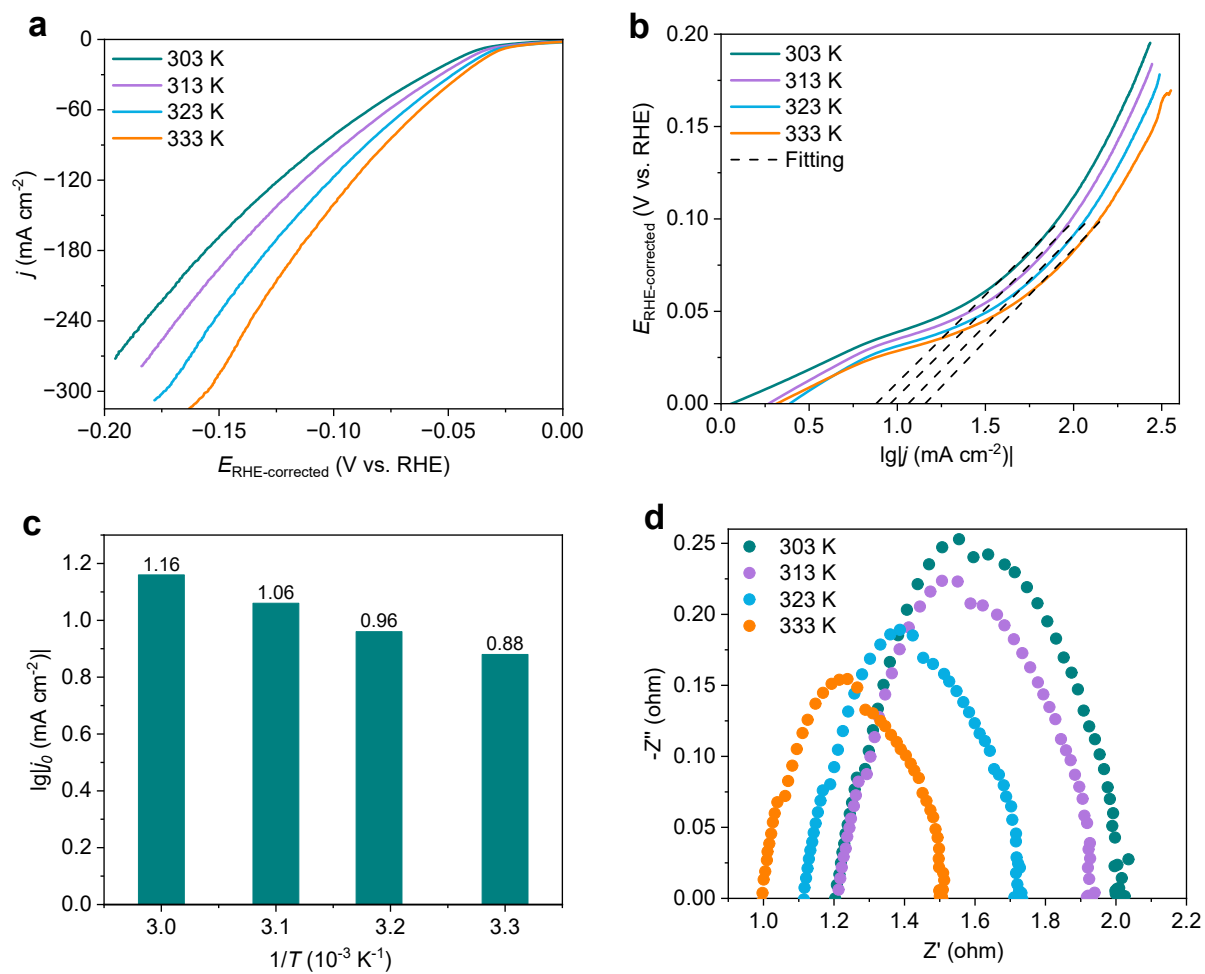


Fig. S12 (a) LSV curves, (b) Tafel plots, (c) exchange current densities, and (d) Nyquist plots of *d*-Ru-ZnO-900 in HER at 303, 313, 323, and 333 K.

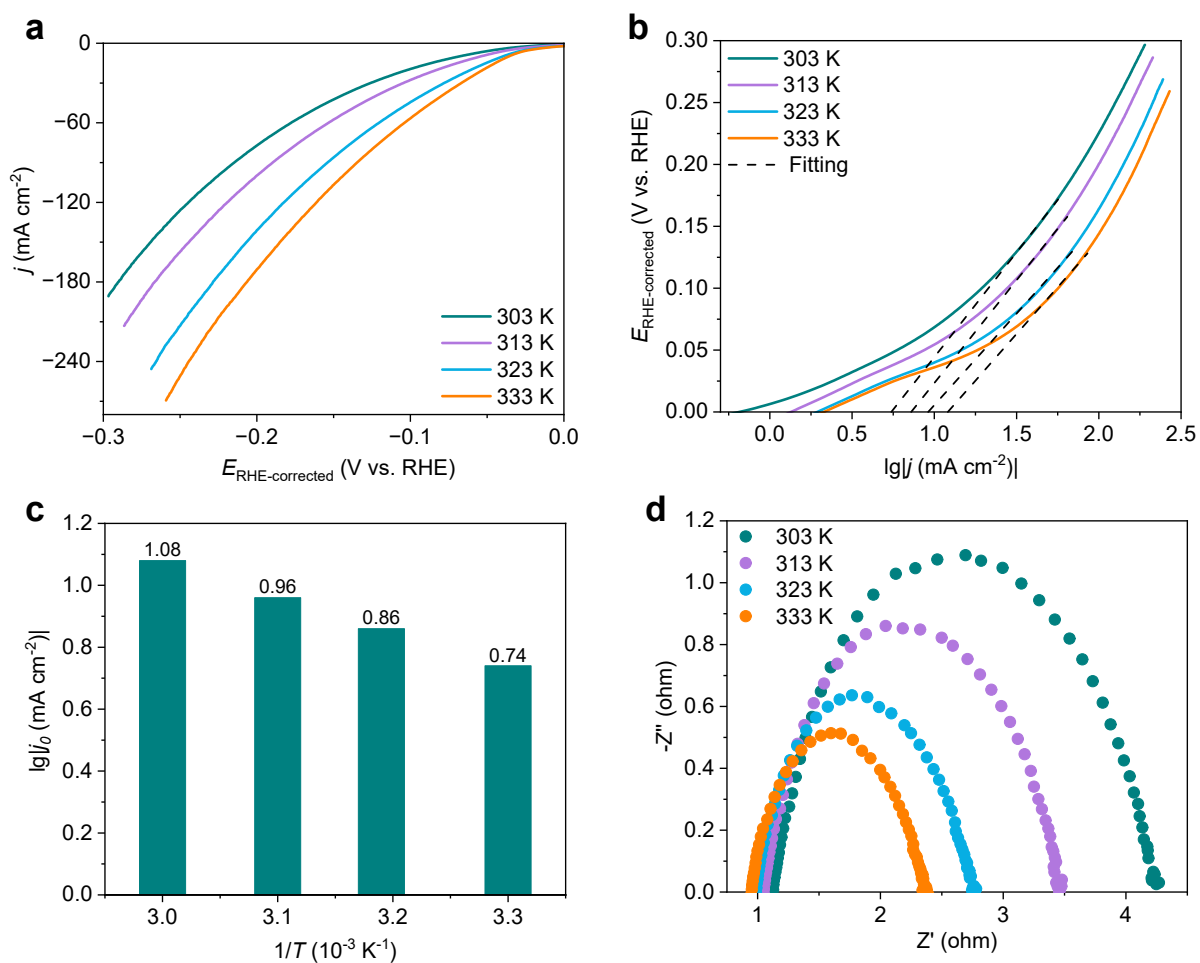


Fig. S13 (a) LSV curves, (b) Tafel plots, (c) exchange current densities, and (d) Nyquist plots of *d*-Ru-ZnO-920 in HER at 303, 313, 323, and 333 K.

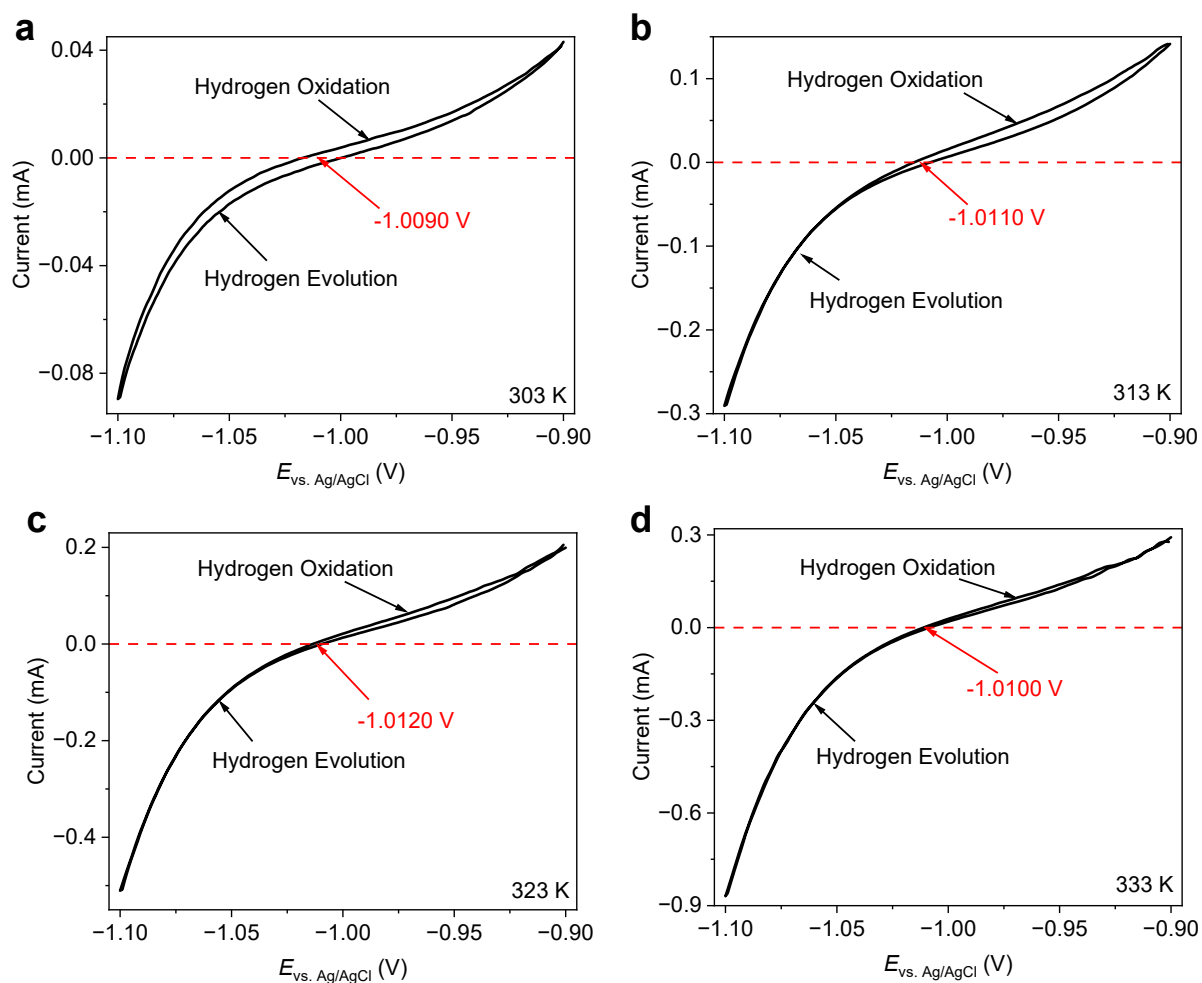


Fig. S14 RHE calibration results of the Ag/AgCl (3.5 mol L^{-1} KCl) reference electrode in 1 mol L^{-1} KOH at a scan rate of 1 mV s^{-1} using a Pt plate (1 cm^2 dipped into the solution) as working and counter electrodes under (a) 303 K, (b) 313 K, (c) 323 K, and (d) 333 K.

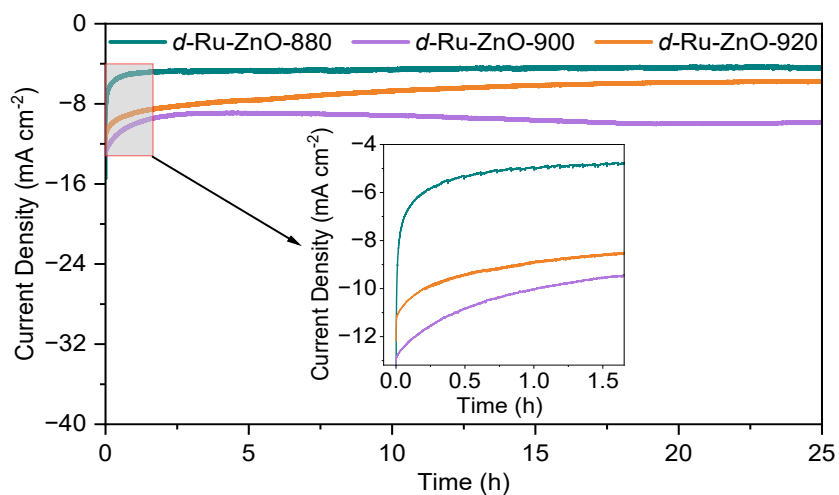


Fig. S15 Comparison of time-dependent current density curves of *d*-Ru-ZnO-880, *d*-Ru-ZnO-900, and *d*-Ru-ZnO-920 under 10 mA cm⁻².

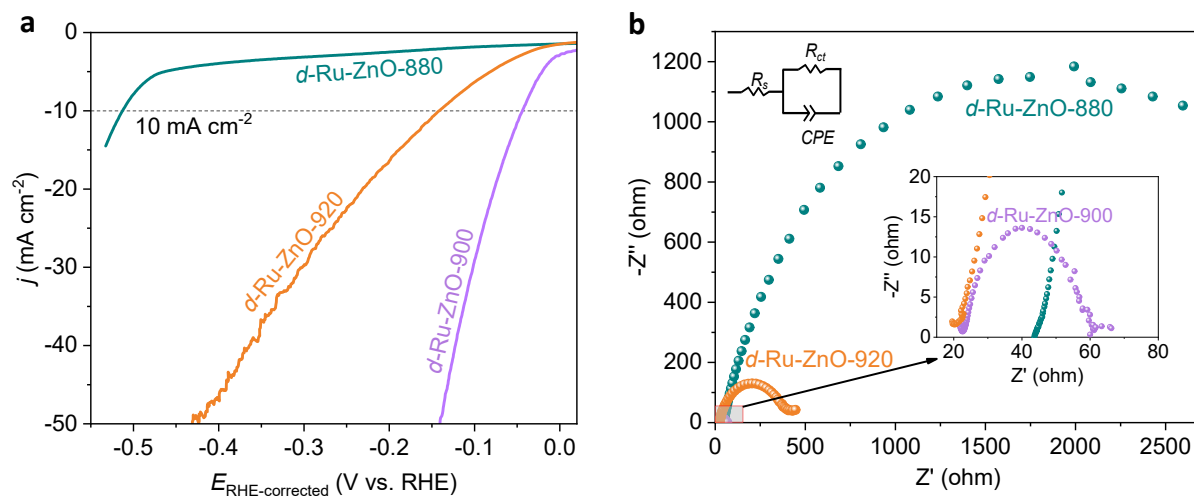


Fig. S16 HER results of *d*-Ru-ZnO-880, *d*-Ru-ZnO-900, and *d*-Ru-ZnO-920 coated on glassy carbon electrode. (a) LSV curves in 1 mol L⁻¹ KOH at a scan rate of 5 mV s⁻¹; (d) Nyquist plots with an enlarged view of rectangular area.

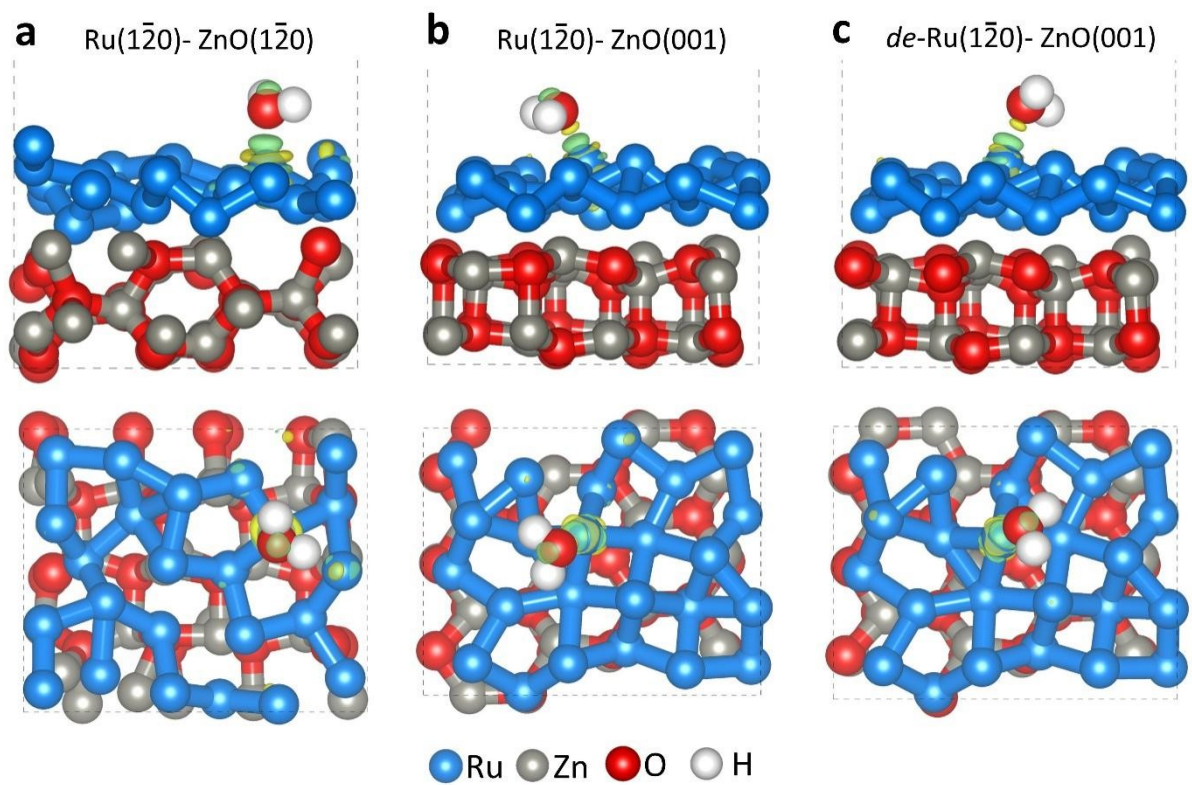


Fig. S17 Optimized differential charge density of adsorbed H₂O on (a) Ru($1\bar{2}0$)-ZnO($1\bar{2}0$), (b) Ru($1\bar{2}0$)-ZnO(001), and (c) *de*-Ru($1\bar{2}0$)-ZnO(001) models. Isosurface = $\pm 0.005 e \text{ \AA}^{-3}$. Yellow and green regions represent electron accumulation and depletion, respectively.

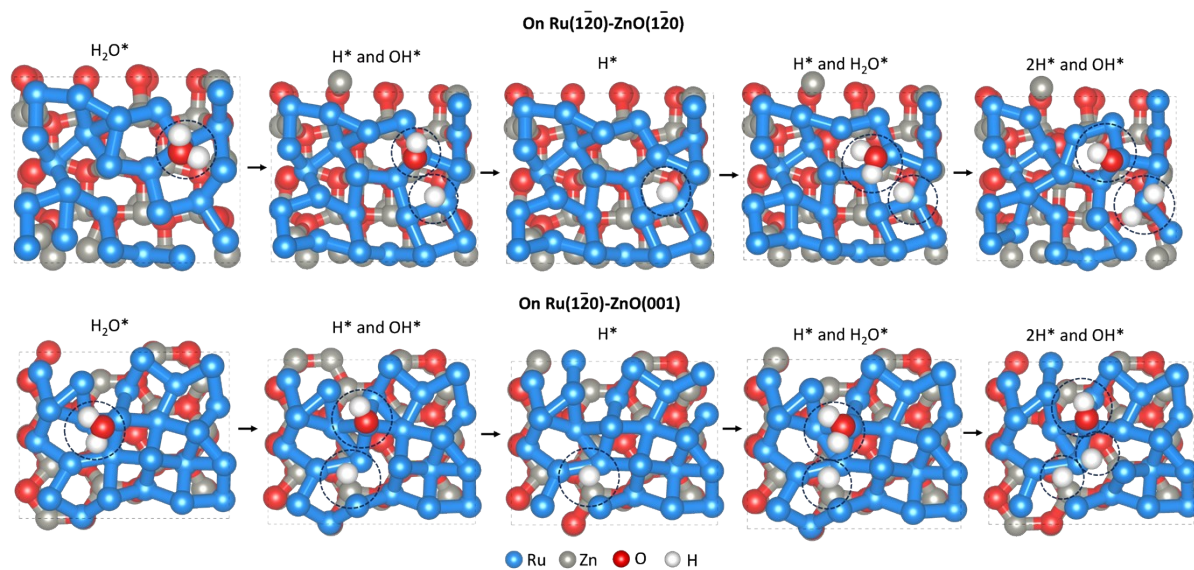


Fig. S18 Optimized adsorption configurations of HER intermediates in the Volmer-Heyrovsky process on Ru(120)-ZnO(120) and Ru(120)-ZnO(001) models (Top view).

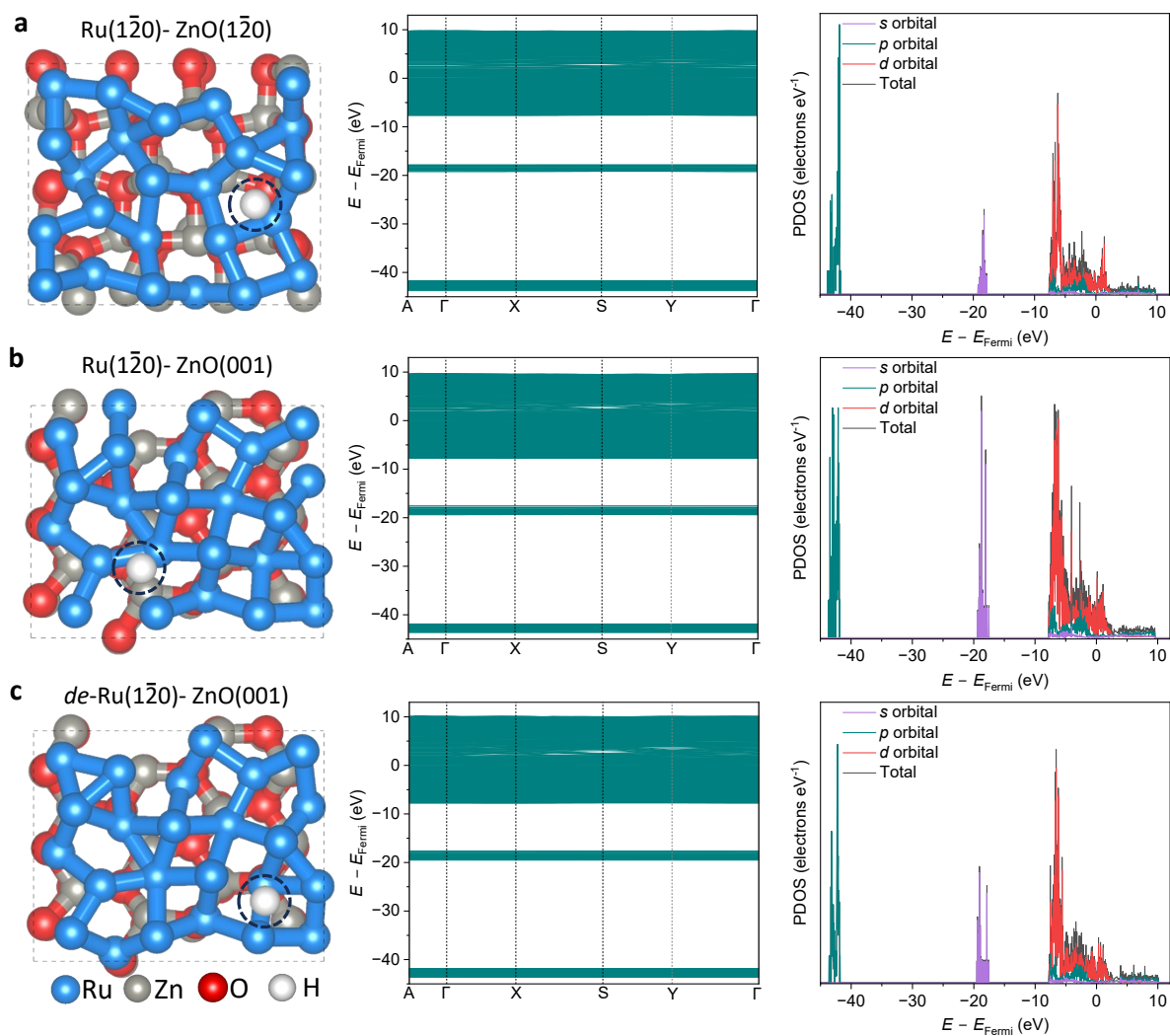


Fig. S19 Top view of optimized adsorption configuration of H^* (left panel), band gap after H^* adsorption (middle panel), and projected electronic density of states after H^* adsorption (right panel) on (a) $\text{Ru}(1\bar{2}0)\text{-ZnO}(1\bar{2}0)$, (b) $\text{Ru}(1\bar{2}0)\text{-ZnO}(001)$, and (c) $de\text{-Ru}(1\bar{2}0)\text{-ZnO}(001)$ models.

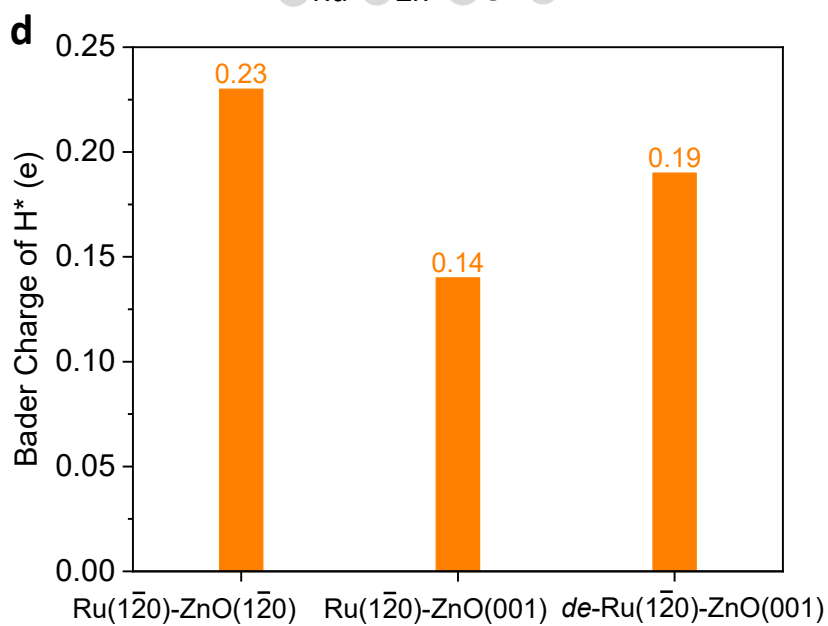
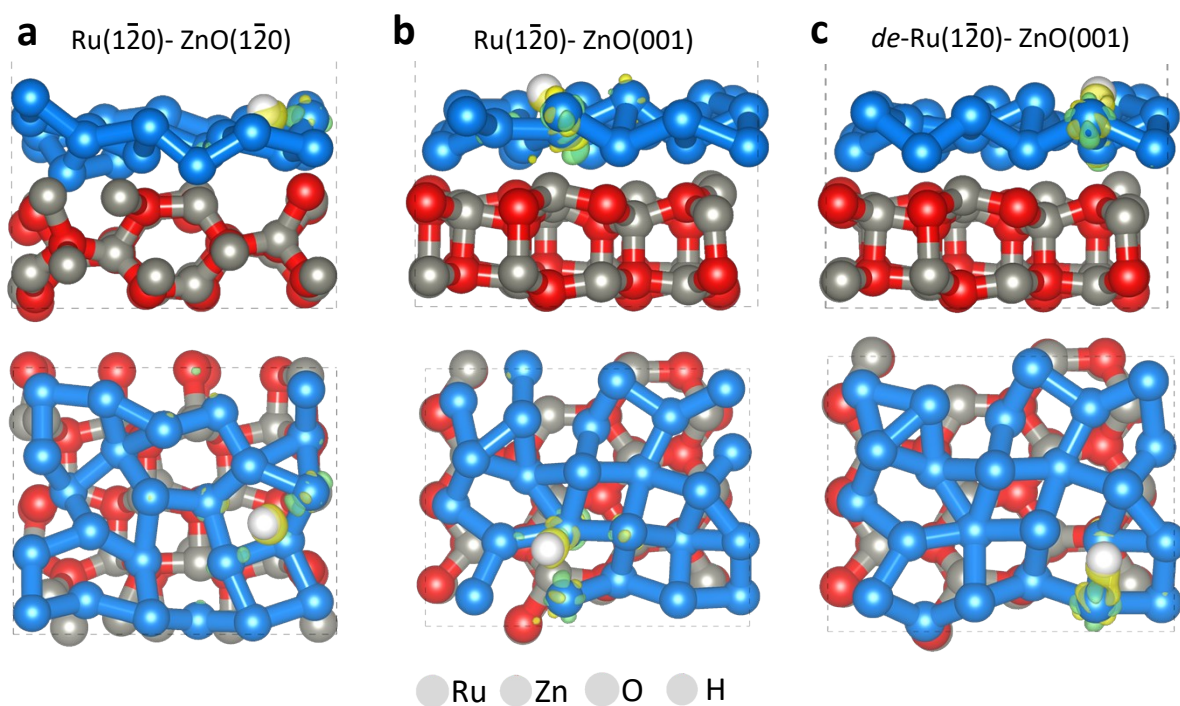


Fig. S20 Optimized differential charge densities of adsorbed H* on (a) Ru($\bar{1}\bar{2}0$)-ZnO($\bar{1}\bar{2}0$), (b) Ru($\bar{1}\bar{2}0$)-ZnO(001), and (c) *de*-Ru($\bar{1}\bar{2}0$)-ZnO(001) models (isosurface: $\pm 0.005 e \text{ \AA}^{-3}$, yellow and green regions represent electron accumulation and depletion, respectively); (d) Bader charges of adsorbed H* on Ru($\bar{1}\bar{2}0$)-ZnO($\bar{1}\bar{2}0$), Ru($\bar{1}\bar{2}0$)-ZnO(001), and *de*-Ru($\bar{1}\bar{2}0$)-ZnO(001) models.

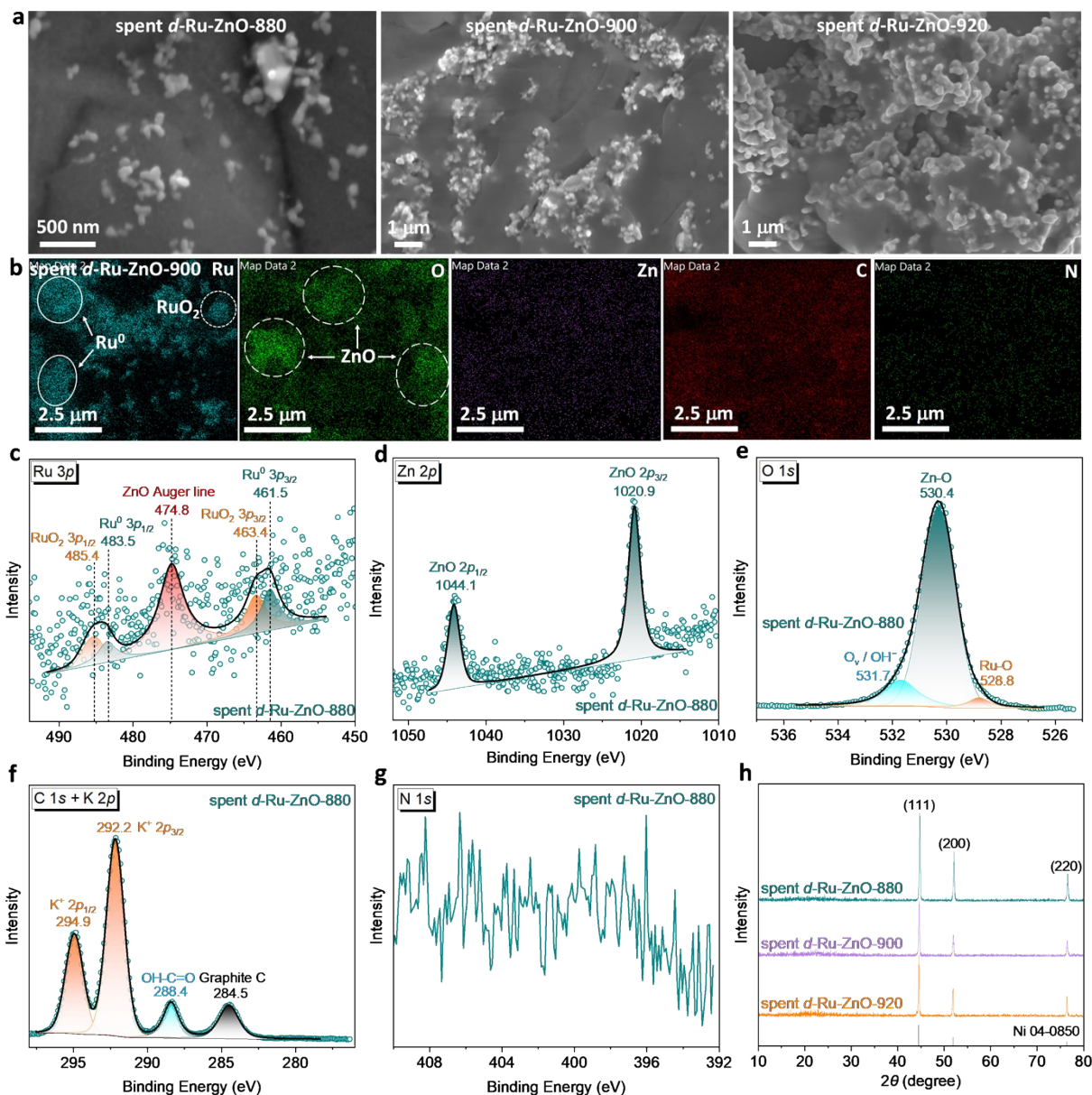


Fig. S21 (a) SEM images of spent *d*-Ru-ZnO-880, spent *d*-Ru-ZnO-900, and spent *d*-Ru-ZnO-920; (b) EDX mapping images of Ru, O, Zn, C, and N of spent *d*-Ru-ZnO-900; (c) Ru 3p, (d) Zn 2p, (e) O 1s, (f) C 1s and K 2p, and (g) N 1s XPS spectra of spent *d*-Ru-ZnO-880; (h) Powder XRD patterns of spent *d*-Ru-ZnO-880, spent *d*-Ru-ZnO-900, and spent *d*-Ru-ZnO-920.

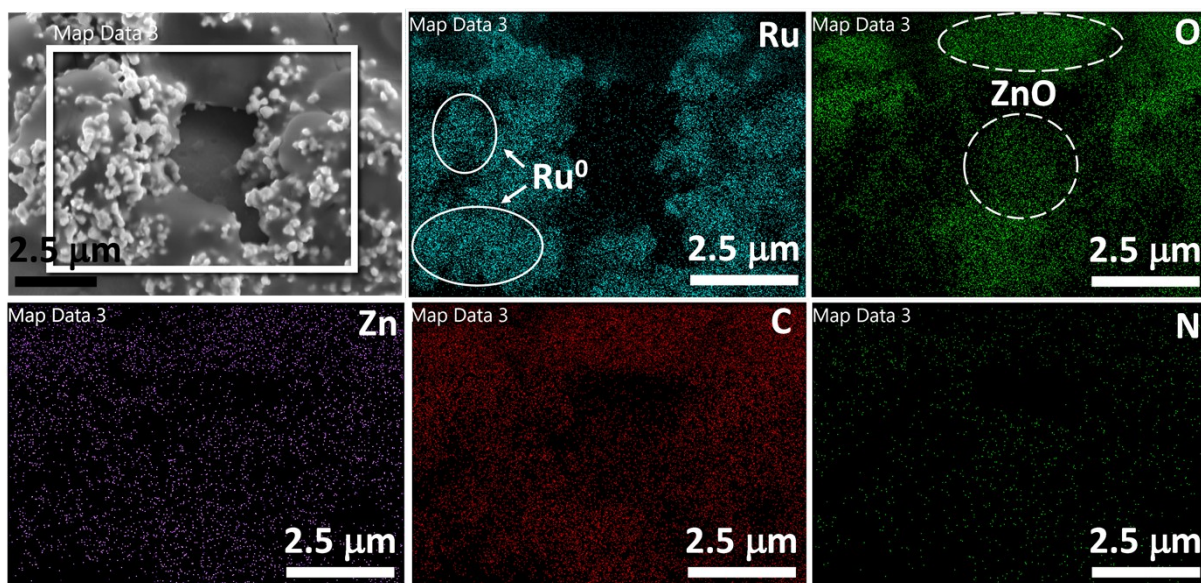


Fig. S22 SEM and corresponding EDX mapping images of Ru, O, Zn, C, and N of spent *d*-Ru-ZnO-920.

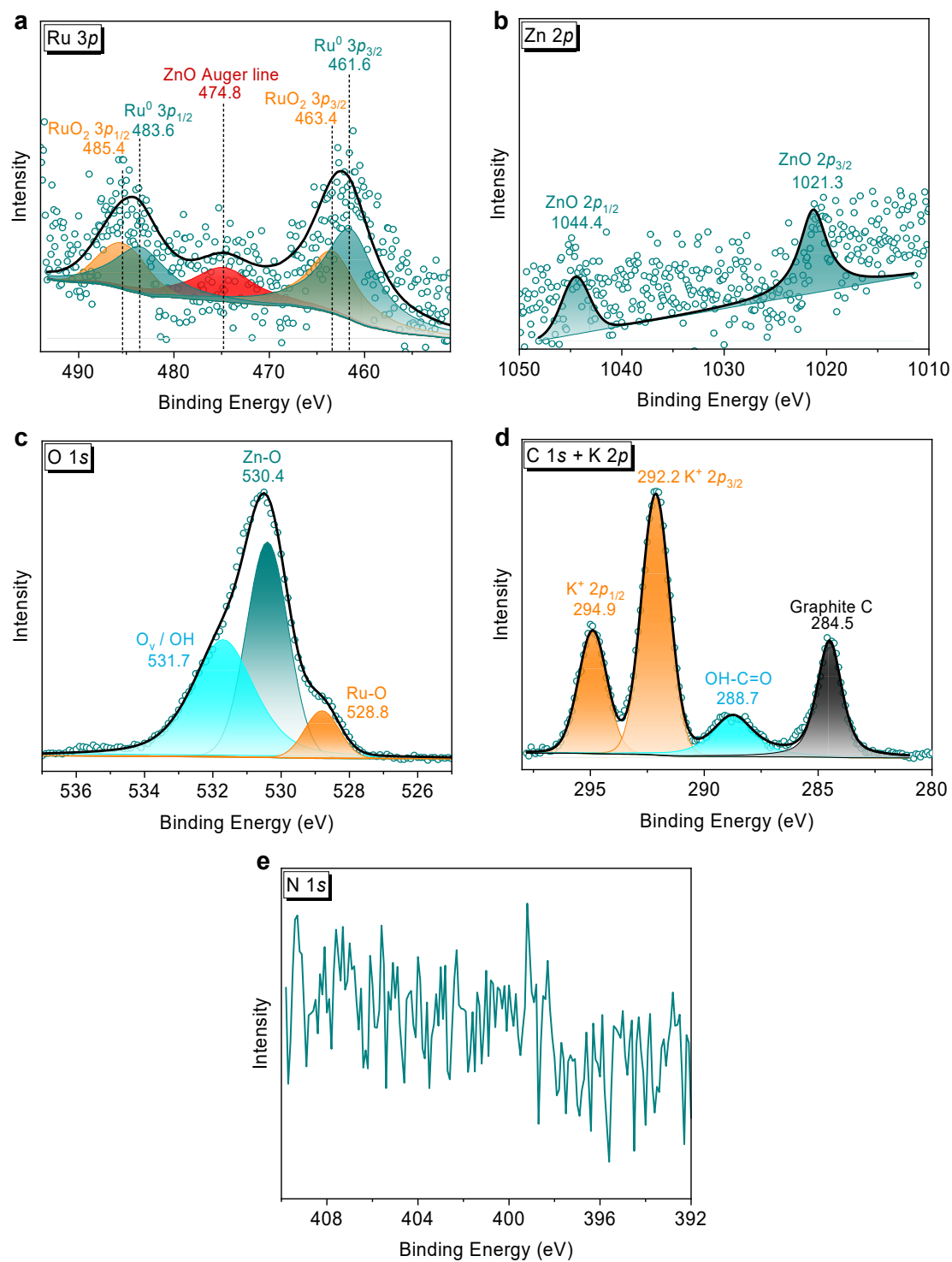


Fig. S23 (a) Ru 3p, (b) Zn 2p, (c) O 1s, (d) C 1s and K 2p, and (e) N 1s XPS spectra of the *d*-Ru-ZnO-900 catalyst after a 50-hour durability test.

Table S1. Physicochemical parameters of *d*-Ru-ZIF-8, *d*-Ru-ZnO-880, *d*-Ru-ZnO-900, and *d*-Ru-ZnO-920.

Material	Material loading on NF (mg cm ⁻²) ^a	Ru content (wt%) ^b	Zn content (wt%) ^b	Ru: Zn bulk molar ratio ^b	<i>S</i> _{BET} (m ² g ⁻¹)	<i>d</i> _{pore} (nm)	<i>V</i> _{pore} (cm ³ g ⁻¹)
Ru-ZIF-8	n.m. ^c	n.m.	n.m.	n.m.	161	9.8	0.39
<i>d</i> -Ru-ZnO-880	1.0	8.8	33.7	0.17	24	5.4	0.03
<i>d</i> -Ru-ZnO-900	1.0	11.5	38.6	0.19	42	5.6	0.06
<i>d</i> -Ru-ZnO-920	1.0	8.2	38.0	0.14	44	4.8	0.05

^a Determined by a weighing method.

^b Determined by ICP–AES.

^c n.m.: not measured.

Table S2. Fitting results of Zn 2*p* and Ru 3*p* spectra of *d*-Ru-ZnO-880, *d*-Ru-ZnO-900, and *d*-Ru-ZnO-920.

Sample	ZnO (eV)		ZnO Auger line (eV)	Ru ⁰ (eV)		RuO ₂ (eV)	
	2 <i>p</i> _{3/2}	2 <i>p</i> _{1/2}		3 <i>p</i> _{3/2}	3 <i>p</i> _{1/2}	3 <i>p</i> _{3/2}	3 <i>p</i> _{1/2}
<i>d</i> -Ru-ZnO-880	1021.3	1044.4	474.8	461.5	483.5	463.4	485.4
<i>d</i> -Ru-ZnO-900	1021.3	1044.4	474.8	461.6	483.6	463.4	485.4
<i>d</i> -Ru-ZnO-920	1021.3	1044.4	474.8	461.7	486.7	463.4	485.4

Table S3. Fitting results of Ru 3d and C 1s spectra of *d*-Ru-ZnO-880, *d*-Ru-ZnO-900, and *d*-Ru-ZnO-920.

Sample	Ru ⁰ (eV)		RuO ₂ (eV)		Graphite C (eV)	C=O (eV)
	3d _{5/2}	3d _{3/2}	3d _{5/2}	3d _{3/2}		
<i>d</i> -Ru-ZnO-880	280.2	284.4	281.6	285.8	284.5	287.5
<i>d</i> -Ru-ZnO-900	280.3	284.5	281.6	285.8	284.5	287.5
<i>d</i> -Ru-ZnO-920	280.4	284.6	281.6	285.8	284.5	287.5

Table S4. Crystal parameters of Ru and ZnO.

	Ru			ZnO		
	Experimental value ¹³	Computed value	Deviation	Experimental value ¹⁴	Computed value	Deviation
a (Å)	2.724	2.717	0.3%	3.254	3.288	1.0%
b (Å)	2.724	2.717	0.3%	3.254	3.288	1.0%
c (Å)	4.317	4.303	0.3%	5.238	5.305	1.3%
α (°)	90	90	0	90	90	0
β (°)	90	90	0	90	90	0
γ (°)	120	120	0	120	120	0

Table S5. Model parameters in DFT calculations.

	Ru(1 $\bar{2}$ 0)-ZnO(1 $\bar{2}$ 0)	Ru(1 $\bar{2}$ 0)-ZnO(001)	<i>de</i> -Ru(1 $\bar{2}$ 0)-ZnO(001)
<i>a</i> (Å)	12.148	12.149	12.149
<i>b</i> (Å)	10.012	9.638	9.638
<i>c</i> (Å) ^a	22.506	22.382	22.382
Number of valence electrons	768	768	767
Number of atoms	72	72	72
	(Ru: 24, Zn: 24, O: 24)	(Ru: 24, Zn: 24, O: 24)	(Ru: 24, Zn: 24, O: 24)

^a *c*-direction contains a 15 Å-thick vacuum layer.

Table S6. Band gap scanning path in the Brillouin zone (the Γ -spot is the center, fractional coordinates).²⁰

Label	k_1	k_2	k_3
Γ	0	0	0
A	0	0	0.5
X	0.5	0	0
S	0.5	0.5	0
Y	0	0.5	0

Table S7. EIS fitting results of *c*-Ru-ZnO-900, *o*-Ru-ZnO-900, *d*-Ru-ZnO-880, *d*-Ru-ZnO-900, *d*-Ru-ZnO-920, and Pt/C benchmark in HER.

Resistance (Ω)	<i>c</i> -Ru-ZnO-900		<i>o</i> -Ru-ZnO-900		<i>d</i> -Ru-ZnO-880		<i>d</i> -Ru-ZnO-900		<i>d</i> -Ru-ZnO-920		Pt/C	
	Value	Error	Value	Error								
R_s	1.7	2.0%	1.1	1.2%	1.3	2.4%	1.2	0.3%	1.2	0.4%	1.5	0.6%
R_{ct}	129.0	1.0%	92.2	1.7%	101.3	1.7%	1.6	0.6%	4.5	0.5%	0.7	5.8%
CPE-T	0.003	1.1%	0.005	1.9%	0.005	1.6%	0.005	3.3%	0.004	2.1%	0.2	12.7%
CPE-P	0.8	0.4%	0.8	0.5%	0.8	0.6%	0.8	0.7%	0.8	0.4%	0.5	5.3%

Table S8. ECSA of *c*-Ru-ZnO-900, *o*-Ru-ZnO-900, *d*-Ru-ZnO-880, *d*-Ru-ZnO-900, and *d*-Ru-ZnO-920.

Sample	<i>c</i> -Ru-ZnO-900	<i>o</i> -Ru-ZnO-900	<i>d</i> -Ru-ZnO-880	<i>d</i> -Ru-ZnO-900	<i>d</i> -Ru-ZnO-920
C_{dl} (mF cm ⁻²)	2.5	2.7	1.7	9.2	3.8
ECSA (cm ²)	62.5	67.5	42.5	230	95

Table S9. Comparison of overpotentials (η_{10} and η_{50}) and charge transfer resistances (R_{ct}) of *d*-Ru-ZnO-880, *d*-Ru-ZnO-900, and *d*-Ru-ZnO-920 coated on nickel foam and glassy carbon electrodes.

Catalysts	NF ^a (mV)		R_{ct}^a (Ω)	GC ^b (mV)		R_{ct}^b (Ω)
	η_{10}	η_{50}		η_{10}	η_{50}	
<i>d</i> -Ru-ZnO-880	230.4	343.2	101.3	512.9	n.m. ^c	3269.0
<i>d</i> -Ru-ZnO-900	25.0	96.9	1.6	44.2	140.7	36.3
<i>d</i> -Ru-ZnO-920	97.5	197.9	4.5	141.9	430.9	370.4

^a Results of catalysts coated on nickel foam substrate.

^b Results of catalysts coated on glassy carbon electrode.

^c n.m.: too large to measure.

Table S10. Comparison of *d*-Ru-ZnO-900 constituents before and after durability test determined by ICP–AES.

Catalyst	Ru content (wt%)	Zn content (wt%)	Ru: Zn molar ratio
Fresh <i>d</i> -Ru-ZnO-900	11.5	38.6	0.19
<i>d</i> -Ru-ZnO-900 after 50 h	24.7	20.2	0.79

References

- 1 S. C. Huang, Y. Y. Meng, Y. F. Cao, F. Yao, Z. J. He, X. X. Wang, H. Pan and M. M. Wu, Amorphous NiWO₄ nanoparticles boosting the alkaline hydrogen evolution performance of Ni₃S₂ electrocatalysts, *Appl. Catal. B: Environ.*, 2020, **274**, 119120.
- 2 B. Fei, Z. L. Chen, J. X. Liu, H. B. Xu, X. X. Yan, H. L. Qing, M. Chen and R. B. Wu, Ultrathinning nickel sulfide with modulated electron density for efficient water splitting, *Adv. Energy Mater.*, 2020, **10**, 2001963.
- 3 D. B. Jia, L. L. Han, Y. Li, W. J. He, C. C. Liu, J. Zhang, C. Chen, H. Liu and H. L. Xin, Optimizing electron density of nickel sulfide electrocatalysts through sulfur vacancy engineering for alkaline hydrogen evolution, *J. Mater. Chem. A*, 2020, **8**, 18207–18214.
- 4 Z. C. Wu, Z. X. Zou, J. S. Huang and F. Gao, Fe-doped NiO mesoporous nanosheets array for highly efficient overall water splitting, *J. Catal.*, 2018, **358**, 243–252.
- 5 L. Yu, I. K. Mishra, Y. L. Xie, H. Q. Zhou, J. Y. Sun, J. Q. Zhou, Y. Z. Ni, D. Luo, F. Yu, Y. Yu, S. Chen and Z. F. Ren, Ternary Ni_{2(1-x)}Mo_{2x}P nanowire arrays toward efficient and stable hydrogen evolution electrocatalysis under large-current-density, *Nano Energy*, 2018, **53**, 492–500.
- 6 Y. Zhang, J. L. Fu, H. Zhao, R. J. Jiang, F. Tian and R. J. Zhang, Tremella-like Ni₃S₂/MnS with ultrathin nanosheets and abundant oxygen vacancies directly used for high speed overall water splitting, *Appl. Catal. B: Environ.*, 2019, **257**, 117899.
- 7 J. Kibsgaard, C. Tsai, K. Chan, J. D. Benck, J. K. Nørskov, F. Abild-Pedersen and T. F. Jaramillo, Designing an improved transition metal phosphide catalyst for hydrogen evolution using experimental and theoretical trends, *Energy Environ. Sci.*, 2015, **8**, 3022–3029.
- 8 G. Kresse and D. Joubert, From ultrasoft pseudopotentials to the projector augmented-wave method, *Phys. Rev. B*, 1999, **59**, 1758.
- 9 G. Kresse and J. Furthmüller, Efficiency of ab-initio total energy calculations for metals and semiconductors using a plane-wave basis set, *Comput. Mater. Sci.*, 1996, **6**, 15–50.
- 10 A. D. Becke, Perspective: Fifty years of density-functional theory in chemical physics, *J. Chem. Phys.*, 2014, **140**, 18A301.

- 11 M. T. Yu, S. Y. Yang, C. Z. Wu and N. Marom, Machine learning the Hubbard U parameter in DFT+ U using Bayesian optimization, *npj Comput. Mater.*, 2020, **6**, 180.
- 12 S. Grimme, J. Antony, S. Ehrlich and H. Krieg, A consistent and accurate *ab initio* parametrization of density functional dispersion correction (DFT-D) for the 94 elements H-Pu, *J. Chem. Phys.*, 2010, **132**, 154104.
- 13 Q. M. Phung, G. Pourtois, J. Swerts, K. Pierloot and A. Delabie, Atomic layer deposition of ruthenium on ruthenium surfaces: A theoretical study, *J. Phys. Chem. C*, 2015, **119**, 6592–6603.
- 14 W. Zhou, Y. Y. Liu, J. F. Guo and P. Wu, Electronic structure and optical properties of V- and Nb-doped ZnO from hybrid functional calculations, *J. Alloys Compd.*, 2015, **621**, 423–427.
- 15 G. S. Shao, Work function and electron affinity of semiconductors: Doping effect and complication due to fermi level pinning, *Energy Environ. Mater.*, 2021, **4**, 273–276.
- 16 J. K. Nørskov, F. Studt, F. Abild-pedersen and T. Bligaard, *Fundamental Concepts in Heterogeneous Catalysis*, John Wiley & Sons, New Jersey, 2015.
- 17 H. Y. Yang, M. Driess and P. W. Menezes, Self-supported electrocatalysts for practical water electrolysis, *Adv. Energy Mater.*, 2021, **11**, 2102074.
- 18 V. Wang, N. Xu, J.-C. Liu, G. Tang and W.-T. Geng, VASPKIT: A user-friendly interface facilitating high-throughput computing and analysis using VASP code, *Comput. Phys. Commun.*, 2021, **267**, 108033.
- 19 B. Fei, Z. L. Chen, J. X. Liu, H. B. Xu, X. X. Yan, H. L. Qing, M. Chen and R. B. Wu, Ultrathinning nickel sulfide with modulated electron density for efficient water splitting, *Adv. Energy Mater.*, 2020, **10**, 2001963.
- 20 Y. Hinuma, G. Pizzi, Y. Kumagai, F. Oba and I. Tanaka, Band structure diagram paths based on crystallography, *Comput. Mater. Sci.*, 2017, **10**, 140–184.

References for electrocatalytic performance comparison in Fig. 8j:

- S1 M. J. Qu, Y. M. Jiang, M. Yang, S. Liu, Q. F. Guo, W. Shen, M. Li and R. X. He, Regulating electron density of NiFe-P nanosheets electrocatalysts by a trifle of Ru for high-efficient overall water splitting, *Appl. Catal. B: Environ.*, 2020, **263**, 118324.
- S2 W. Li, B. M. Feng, L. Y. Yi, J. Y. Li and W. H. Hu, Highly efficient alkaline water splitting with Ru-doped Co-V layered double hydroxide nanosheets as a bifunctional electrocatalyst, *ChemSusChem.*, 2021, **14**, 730–737.
- S3 Y. Y. Ma, Y. Ha, L. Q. Chen, Z. Q. An, L. Z. Xing, Z. N. Wang and Z. M. Li, Electrochemically induced Ru/CoOOH synergistic catalyst as bifunctional electrode materials for alkaline overall water splitting, *Small*, 2024, **2020**, 2311884.
- S4 W. Xia, M. Y. Ma, X. Y. Guo, D. J. Cheng, D. F. Wu and D. Cao, Fabricating Ru atom-doped novel FeP₄/Fe₂PO₅ heterogeneous interface for overall water splitting in alkaline environment, *ACS Appl. Mater. Interfaces*, 2023, **15**, 44827–44838.
- S5 J.-X. Guo, D.-Y. Yan, K.-W. Qiu, C. Mu, D. Jiao, J. Mao, H. Wang and T. Ling, High electrocatalytic hydrogen evolution activity on a coupled Ru and CoO hybrid electrocatalyst, *J. Energy Chem.*, 2019, **37**, 143–147.
- S6 L. Qian, Y. Zhu, H. T. Hu, Y. H. Zheng, Z. Y. Yuan, Y. T. Dai, T. Zhang, D. Y. Yang, S. L. Xue and F. X. Qiu, Unique sandwich-cookie-like nanosheet array heterojunction bifunctional electrocatalyst towards efficient overall water/seawater splitting, *J. Colloid Interf. Sci.*, 2024, **669**, 935–943.
- S7 Y. Jiang, Y. N. Mao, Y. M. Jiang, H. Liu, W. Shen, M. Li and R. X. He, Atomic equidistribution enhanced RuIr electrocatalysts for overall water splitting in the whole pH range, *Chem. Eng. J.*, 2022, **450**, 137909.
- S8 S. D. Liu, L. L. Liu, J. J. Liu, Y. Xiang, L. J. Gao, F. Fu, X. M. Gao and X. Jian, Mo₂TiC₂T_x MXene-supported Ru/Ni–NiO as an electrocatalyst for the pH-universal hydrogen evolution reaction, *ACS Appl. Nano Mater.*, 2023, **6**, 22192.
- S9 M. Z. You, X. Du, X. H. Hou, Z. Y. Wang, Y. Zhou, H. P. Ji, L. Y. Zhang, Z. T. Zhang, S. S. Yi and D. L. Chen, In-situ growth of ruthenium-based nanostructure on carbon cloth for

- superior electrocatalytic activity towards HER and OER, *Appl. Catal. B: Environ.*, 2022, **317**, 121729.
- S10 J. M. Zhang, X. P. Xu, L. Yang, D. J. Cheng and D. P. Cao, Single-atom Ru doping induced phase transition of MoS₂ and S vacancy for hydrogen evolution reaction, *Small Methods*, 2019, **3**, 1900653.
- S11 Y. J. Wang, W. J. Luo, H. J. Li and C. W. Cheng, Ultrafine Ru nanoclusters supported on N/S doped macroporous carbon spheres for efficient hydrogen evolution reaction, *Nanoscale Adv.*, 2021, **3**, 5068–5074.
- S12 M. Liu, Y. Xu, S. L. Liu, S. L. Yin, M. Y. Liu, Z. Q. Wang, X. N. Li, L. Wang and H. J. Wang, Phosphorus-modified ruthenium–tellurium dendritic nanotubes outperform platinum for alkaline hydrogen evolution, *J. Mater. Chem. A*, 2021, **9**, 5026–5032.
- S13 J. M. Cen, P.-K. Shen and Y. F. Zeng, Ru doping NiCoP hetero-nanowires with modulated electronic structure for efficient overall water splitting, *J. Colloid Interf. Sci.*, 2022, **610**, 213–220.
- S14 L. B. Li, J. K. Qu, L. Zhang, L. T. Wei, J. Z. Su and L. J. Guo, RuSe₂ and CoSe₂ nanoparticles incorporated nitrogen-doped carbon as efficient trifunctional electrocatalyst for zinc–air batteries and water splitting, *ACS Appl. Mater. Interfaces*, 2024, **16**, 24660–24670.
- S15 Z. Y. He, Y. Q. Chen, J. Y. Tian, X. Y. Cheng, M. Q. Xia, C. Zhou, Y. Zhang, X. Z. Wang, L. J. Yang, Q. Wu and Z. Hu, Highly dispersed quasi-1 nm ruthenium nanoclusters on hierarchical nitrogen-doped carbon nanocages constructed by surface-constrained sintering for alkaline hydrogen evolution, *ACS Appl. Nano Mater.*, 2024, **7**, 11882–11889.
- S16 H. Liu, Y. Jiang, Y. N. Mao, Y. M. Jiang, W. Shen, M. Li and R. X. He, The role of various components in Ru-NiCo alloys in boosting the performance of overall water splitting, *J. Colloid Interf. Sci.*, 2023, **633**, 189–198.
- S17 Y. Hou, Z. Qin, X. Han, Y. X. Liu, W. Zhang, X. Q. Cao, Y. Y. Cao, J.-P. Lang and H. W. Gu, Thermal evaporation-driven fabrication of Ru/RuO₂ nanoparticles onto nickel foam for efficient overall water splitting, *Nanoscale*, 2024, **16**, 6662–6668.

- S18 Q.-Q. Chen, X. Yang, C.-C. Hou, K. Li and Y. Chen, Inlay of ultrafine Ru nanoparticles into a self-supported Ni(OH)₂ nanoarray for hydrogen evolution with low overpotential and enhanced kinetics, *J. Mater. Chem. A*, 2019, **7**, 11062–11068.
- S19 G. B. Chen, T. Wang, J. Zhang, P. Liu, H. J. Sun, X. D. Zhuang, M. W. Chen and X. L. Feng, Accelerated hydrogen evolution kinetics on NiFe-layered double hydroxide electrocatalysts by tailoring water dissociation active sites, *Adv. Mater.*, 2018, **30**, 1706279.
- S20 B. B. Jiang, Z. Wang, H. Zhao, X. Wang, X. X. Mao, A. J. Huang, X. H. Zhou, K. Yin, K. F. Sheng and J. W. Wang, Ru nanoclusters anchored on boron- and nitrogen-doped carbon for a highly efficient hydrogen evolution reaction in alkaline seawater, *Nanoscale*, 2023, **15**, 19703–19708.
- S21 H. B. Liu, Q. H. Jia, S. Q. Huang, L. Yang, S. T. Wang, L. R. Zheng and D. P. Cao, Ultra-small Ru nanoparticles embedded on Fe–Ni(OH)₂ nanosheets for efficient water splitting at a large current density with long-term stability of 680 hours, *J. Mater. Chem. A*, 2022, **10**, 4817–4824.
- S22 J. P. Sun, Z. Zhao, Z. Z. Li, Z. S. Zhang, R. F. Zhang and X. C. Meng, Ultrafast carbothermal shocking fabrication of cation vacancy-rich Mo doped Ru nanoparticles on carbon nanotubes for high-performance water/seawater electrolysis, *J. Mater. Chem. A*, 2023, **11**, 22430–22440.
- S23 J. Q. Niu, J. Yang, A. I. Channa, E. Ashalley, J. C. Yang, J. Jiang, H. D. Li, H. N. Ji and X. B. Niu, Enhancing the water splitting performance via decorating Co₃O₄ nanoarrays with ruthenium doping and phosphorization, *RSC Adv.*, 2020, **10**, 27235–27241.
- S24 A. Q. Kong, M. Peng, H. Z. Gu, S. C. Zhao, Y. Lv, M. H. Liu, Y. W. Sun, S. D. Dai, Y. Fu, J. L. Zhang and W. Li, Synergetic control of Ru/MXene 3D electrode with superhydrophilicity and superaerophobicity for overall water splitting, *Chem. Eng. J.*, 2021, **426**, 131234.
- S25 Z. X. Wu, Y. Zhao, H. B. Wu, Y. X. Gao, Z. Chen, W. Jin, J. S. Wang, T. Y. Ma and L. Wang, Corrosion engineering on iron foam toward efficiently electrocatalytic overall water splitting powered by sustainable energy, *Adv. Funct. Mater.*, 2021, **31**, 2010437.

- S26 X. Y. Zhang, J. Li, L. W. Yan, S. K. Huang, P. X. Zhang, Z. C. Peng, L. R. Zheng and C. Y. Zhao, Ruthenium decorated 2D N-doped carbon nanocone arrays for pH-universal electrocatalytic hydrogen evolution, *Appl. Surf. Sci.*, 2021, **559**, 149978.
- S27 D. Li, X. L. Shi, S. C. Sun, X. Y. Zheng, D. Tian and D. L. Jiang, Metal–organic framework-derived three-dimensional macropore nitrogen-doped carbon frameworks decorated with ultrafine Ru-based nanoparticles for overall water splitting, *Inorg. Chem.*, 2022, **61**, 9685–9692.